

Self-organised dynamics and emergent shape spaces of active isotropic fluid surfaces

Da Gao,¹ Huayang Sun,¹ Rui Ma,^{1,*} and Alexander Mietke^{2,†}

¹*Department of Physics, College of Physical Science and Technology, Xiamen University, Xiamen 361005, People's Republic of China*

²*Rudolf Peierls Centre for Theoretical Physics, Department of Physics, University of Oxford, Parks Road, Oxford OX1 3PU, United Kingdom*

Theories of self-organised active fluid surfaces have emerged as an important class of minimal models for the shape dynamics of biological membranes, cells and tissues. Here, we develop and apply a variational approach for active fluid surfaces to systematically study the nonlinear dynamics and emergent shape spaces such theories give rise to. To represent dynamic surfaces, we design an arbitrary Lagrangian-Eulerian parameterizations for deforming surfaces. Exploiting the symmetries imposed by Onsager relations, we construct a variational formulation that is based on the entropy production in active surfaces. The resulting dissipation functional is complemented by Lagrange multipliers to relax nonlinear geometric constraints, which allows for a direct computation of steady state solutions of surface shapes and flows. We apply this framework to study the dynamics of open fluid membranes and closed active fluid surfaces, and characterize the space of stationary solutions that corresponding surfaces and flows occupy. Our analysis rationalizes the interplay of first-order shape transitions of internally and externally forced fluid membranes, reveals degenerate regions in stationary shape spaces of mechanochemically active surfaces and identifies a mechanism by which hydrodynamic screening controls the geometry of active surfaces undergoing cell division-like shape transformations.

I. INTRODUCTION

Many crucial processes in living systems rely on the geometric control of two-dimensional structures with fluid-like properties. Membranes, which are critical to regulate traffic into and out of biological cells via endocytosis and exocytosis [1–3], are made of a thin lipid bilayer sheet. These sheets behave as two-dimensional fluids [4] due to weak hydrophobic lateral interactions among lipids [5, 6], while orientational order in lipid packing allows membranes to resist bending. The cortex of eukaryotic cells is a thin polymer filament network beneath the cell membrane of eukaryotic cells [5]. Turnover of filaments and cross-linkers endows the cortex on time scales of seconds with viscous fluid properties [7]. Active mechanical forces generated by motor proteins lead to cortical flows [8, 9], and play a crucial role in maintaining cell shape and enabling dynamic cellular processes such as migration and division [7, 9–12]. Epithelial tissues are effectively two-dimensional cell monolayers that are critical for embryonic development and morphogenesis [10, 13]. This role is facilitated by active cellular processes that allow epithelial tissues to autonomously change their shape [14]. Cellular rearrangements, cell division and cell death lead to viscous material properties on the time scale of hours [15]. The ability to resist bending plays an important role in both the cellular cortex [16] and in epithelial tissues [17].

Given the abundance of fluid surfaces involved in the shape-regulation of cells and tissues minimal models of self-organizing active fluid surfaces have become an essential framework to understand the emergence of form in living systems [18–22]. An often encountered bottleneck in investigating such theories is the inevitably nonlinear nature of sur-

face force and moment balance equations that involve *a priori* unknown, or even dynamic, domain geometries. Restricting oneself to axisymmetric geometries and surfaces that exhibit a purely passive response to bending, this bottleneck has been addressed within a historical body of work starting from the formulation of the Helfrich bending free energy [23–25] over the derivation of highly non-linear shape equations [26, 27] to the formulation of a variational approach that converts the shape equation into a tractable boundary value problem [28–31]. The success of this variational formulation in explaining many experimental observations [32–38] arose from its ability to systematically characterize the space of stationary surface shapes.

Active materials can in general not be described in terms of an energy functional, which raises the question if and how variational formulations – analog to those previously developed for passive membranes – can be systematically developed for out-of-equilibrium fluid surfaces. A promising route to address this question has been pioneered in [39–41] using Onsager’s variational principle. In this formulation, a Rayleigh functional is constructed that includes the free energy change rate and dissipative energy losses. Variation of the Rayleigh functional then gives rise to a set of dynamic equations [41]. However, while suitable expression for common contributions, such as viscous dissipation, can essentially be guessed there exists currently no systematic way to start from generalized constitutive laws of active surfaces [18, 42] and formulate a corresponding functional. Additionally, because the minimization of dissipation is not a fundamental principle [43], it is not clear *a priori* that such a functional would exist in all cases.

Here, we build on recent theoretical advances in applying the framework of irreversible thermodynamics to curved and deforming surfaces [18, 42]. Exploiting the symmetries imposed by Onsager relations [44–46], we show that the entropy production of active deforming surfaces derived in these works can indeed be used to construct suitable Rayleigh functionals.

* ruima@xmu.edu.cn

† alexander.mietke@physics.ox.ac.uk

Specifically, variations of the latter give rise to a boundary value problem that is equivalent to the force and moment balance equations for the full set of *a priori* defined constitutive laws, including those describing the out-of-equilibrium maintenance of chemical potentials, and even if both dissipative and reactive couplings are present.

A key numerical challenge when solving the resulting system of equations is that not only the surface geometry, but also its parameterization depends on time. This potentially results in a lack of computational control over the accuracy with which the physical surface can be represented and is often addressed using arbitrary Lagrangian-Eulerian (ALE) parameterizations [47–49]. In this work, we design an ALE parameterization that can directly be integrated into the dissipation functional, facilitates a numerically robust implicit solution of the shape dynamics and ensures points on the deforming surface are mapped to fixed reference coordinates via a simple scaling. This provides us with an integrated framework with which we will study both the dynamics and the space of stationary geometries and flows on deforming active fluid surface undergoing different, biologically relevant shape transformations.

II. DYNAMICS OF PARAMETERIZED CURVED SURFACES

We describe a surface Ω by the vector field $\mathbf{X}(s^1, s^2, t) \subset \mathbb{R}^3$ that is parameterised by two generalised coordinates s^i ($i \in \{1, 2\}$) and time t . Tangent vectors and surface normal are given by $\mathbf{e}_i = \partial_i \mathbf{X}$ and $\mathbf{n} = \mathbf{e}_1 \times \mathbf{e}_2 / |\mathbf{e}_1 \times \mathbf{e}_2|$, respectively, where we denote $\partial_i := \partial / \partial s^i$. Metric tensor and curvature tensors are defined by $g_{ij} = \mathbf{e}_i \cdot \mathbf{e}_j$ and $C_{ij} = -\mathbf{n} \cdot \partial_i \partial_j \mathbf{X}$. The surface area element is given by $dA = \sqrt{g} ds^1 ds^2$, where $g = \det(g_{ij})$. Vector fields on the surface $\mathbf{w} = \mathbf{w}_{\parallel} + \mathbf{w}_{\perp}$ can be expanded in terms of their in-plane components $\mathbf{w}_{\parallel} = w^i \mathbf{e}_i$ and their normal components $\mathbf{w}_{\perp} = w_n \mathbf{n}$. We denote Euclidean representations of metric and curvature tensor by $\mathbf{G} = g_{ij} \mathbf{e}^i \otimes \mathbf{e}^j$ and $\mathbf{C} = C_{ij} \mathbf{e}^i \otimes \mathbf{e}^j$, respectively, and similarly for other tangential tensors.

A. Parameterization dynamics of deforming surfaces

Any motion and deformation of the surface can be described by a local center-of-mass velocity field $\mathbf{v} = v^i \mathbf{e}_i + v_n \mathbf{n}$, where v^i are in-plane flow components and normal components v_n correspond to flows that move the surface or change its shape. The general surface dynamics is given by

$$\frac{d\mathbf{X}}{dt} = \mathbf{v}, \quad (1)$$

where $\frac{d}{dt}(\cdot)$ denotes the total time derivative. A key challenge in solving Eq. (1) is that surface deformations will generally require a parameterization that depends itself on time. To discuss this explicitly, we expand the total time derivative in

Eq. (1), which gives

$$\partial_t \mathbf{X} + q^i \partial_i \mathbf{X} = \mathbf{v}. \quad (2)$$

Intuitively, the components q^i of the coordinate flow $\mathbf{q} = q^i \mathbf{e}_i$ capture the motion of a surface point \mathbf{X} at fixed coordinates s^i , relative to the in-plane center-of-mass velocity $\mathbf{v}_{\parallel} = v^i \mathbf{e}_i$ of that surface point. Formally, defining how the parameterization of a deforming surface evolves over time will define q^i and *vice versa*. For example, a surface point \mathbf{X} at some fixed center-of-mass or material coordinate S moves by definition with the in-plane center-of-mass velocity \mathbf{v}_{\parallel} , such that we must have $q^i = 0$ if the surface is parameterized by material coordinates. This corresponds to a Lagrangian parametrization for which the surface dynamics Eq. (1) becomes $\partial_t \mathbf{X} = \mathbf{v}$ [12, 18, 22]. Another common parametrization choice is to set $q^i = v^i$, corresponding to an Eulerian parametrization, for which the surface dynamics Eq. (1) becomes $\partial_t \mathbf{X} = v_n \mathbf{n}$ [18, 19]. In this case, the in-plane center-of-mass velocity $\mathbf{v}_{\parallel} = v^i \mathbf{e}_i$ dictates how coordinates associated with a given material element change over time. In general, the dynamic dependence $s^i(S, t)$ of generalised coordinates s^i on material coordinates S is related to q^i by

$$q^i = \left. \frac{\partial s^i}{\partial t} \right|_S, \quad (3)$$

and either of the two – $q^i(s^i, t)$ or $s^i(S, t)$ – can in principle be chosen freely and such that the parameterization is neither Lagrangian nor Eulerian. Analogue approaches in “flat” Euclidean space are called arbitrary Lagrangian-Eulerian (ALE) methods [50], a terminology that we will adopt in the present work when extending it to embedded curved surfaces.

B. Conservation laws on ALE-parameterized curved surfaces

To formulate conservation laws and transport equations on ALE-parameterized curved surfaces, one has to determine the dynamics of area integrals of the form

$$F(t) = \int_{\omega(t)} ds^1 ds^2 \sqrt{g} f(s^1, s^2, t), \quad (4)$$

where the integration domain $\omega(t)$ is some coordinate region that parameterizes a fixed set of material elements. Importantly, $\omega(t)$ is only independent of time if Lagrangian material coordinates are used. We show in Appendix C 1 that for an ALE-parameterized curved surface

$$\frac{dF}{dt} = \int_{\Omega} dA \left[\frac{1}{\sqrt{g}} \partial_t (f \sqrt{g}) + \nabla_i (f q^i) \right], \quad (5)$$

where ∇_i denotes the covariant derivative. Using the covariant Stokes theorem [18], the second term can be identified as a boundary term that results from the dynamics of the coordinate region $\omega(t)$. As expected, this boundary contribution vanishes for a Lagrangian parameterization ($q^i = 0$) and it

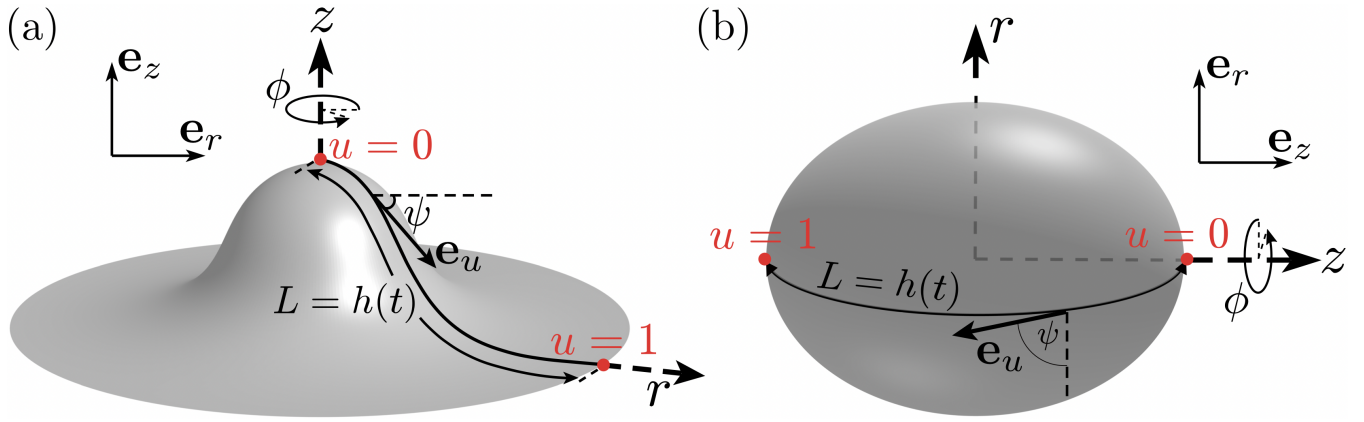


Figure 1. Parameterization of open (a) and closed (b) axisymmetric surfaces $\mathbf{X}(u, \phi, t)$ considered in this work [see Eq. (8)]. A scaling Lagrangian-Eulerian parameterization (Sec. IID) maps fixed mesh coordinates $u \in [0, 1]$ to physical arc length coordinates s on the deforming surface via $s = h(t)u$. ψ denotes the tangent angle and $\mathbf{e}_u = \partial_u \mathbf{X}$ the meridional tangent vector. Cylindrical coordinates (r, ϕ, z) parameterize the embedding Euclidean space. The total length $L = h(t)$ of the meridional outline changes in time as surfaces deform.

can be interpreted as a flux $j_f^i = f v^i$ across the boundary for a Eulerian parameterization ($q^i = v^i$). In general, however, it is not a physical flux but an artefact of any parameterization that is decoupled from the center-of-mass motion of local area elements.

Setting as an example $f = \rho$, where ρ is the mass density of the surface, we have the total mass $F(t) = M(t)$ and mass conservation directly follows from Eq. (5) (Appendix C 2 a). If multiple chemical species α of concentration $c_\alpha(s^1, s^2, t)$ are present, this leads to continuity equations for each species of the form

$$\partial_t c_\alpha + q^i \partial_i c_\alpha + c_\alpha \text{div}(\mathbf{v}) + \text{div}(\mathbf{j}_\alpha) = r_\alpha + J_{n,\alpha}, \quad (6)$$

where $\text{div}(\cdot) := \mathbf{e}^i \cdot \partial_i(\cdot)$ denotes the divergence operator on the surface implying

$$\text{div}(\mathbf{v}) = \nabla_i v^i + C_i^i v_n, \quad (7)$$

$\mathbf{j}_\alpha = j_\alpha^i \mathbf{e}_i$ are diffusive fluxes relative to the in-plane center-of-mass flux $c_\alpha v^i$, r_α denotes chemical reaction rates among species, and $J_{n,\alpha}$ denotes fluxes between the surface and its environment.

C. Deforming axisymmetric surfaces

Purely Lagrangian and Eulerian parameterizations relate the coordinate flow q^i only to the in-plane center-of-mass velocity \mathbf{v}_\parallel and are consequently slave to the systems dynamics, precluding any explicit level of control whenever surface movements and deformations occur. When solving Eq. (1) numerically, this lack of control over the parameterization is typically countered by using an adaptive remeshing [12, 49], which repeatedly interpolates the surface state and effectively resets the parameterization. By integrating surface deformations into the coordinate flow q^i , we develop and apply in the following an approach that reduces the dependence of the parameterization on the surface dynamics to a homogeneous

global scaling, which naturally eliminates the need for flow-dependent remeshing. To make this concrete, we consider a deforming axisymmetric surface described by

$$\mathbf{X}(u, \phi, t) = [r(u, t) \cos \phi, r(u, t) \sin \phi, z(u, t)], \quad (8)$$

where $r(u, t)$ and $z(u, t)$ denote time-dependent components of points on the surface, and $u \in [0, 1]$ and $\phi \in [0, 2\pi]$ are time-independent coordinates we refer to as *mesh coordinates* (Fig. 1). To restrict the following discussion to the essential findings, we consider center of mass flows

$$\mathbf{v}(u, \phi, t) = v^u(u, t) \mathbf{e}_u + v_n(u, t) \mathbf{n}, \quad (9)$$

and refer for a discussion that includes azimuthal flows $\sim v^\phi(u, t) \mathbf{e}_\phi$ to the appendix. The components of the surface dynamics implied by Eqs. (2), (8) and (9) are given by

$$\partial_t r = (v^u - q^u) r' - \frac{z'}{\sqrt{r'^2 + z'^2}} v_n \quad (10)$$

$$\partial_t z = (v^u - q^u) z' + \frac{r'}{\sqrt{r'^2 + z'^2}} v_n, \quad (11)$$

where dashes $'$ denote partial derivatives with respect to u . Reparameterizing the component derivatives $\{r'(u, t), z'(u, t)\} \rightarrow \{(h(u, t), \psi(u, t))\}$, where $h = \sqrt{r'^2 + z'^2}$ and ψ is determined by

$$r' = h \cos \psi \quad (12)$$

$$z' = -h \sin \psi, \quad (13)$$

the shape dynamics Eqs. (10), (11) becomes

$$\partial_t r = (v^u - q^u) h \cos \psi + v_n \sin \psi \quad (14)$$

$$\partial_t z = (q^u - v^u) h \sin \psi + v_n \cos \psi. \quad (15)$$

Note that ψ can be geometrically interpreted as the tangent angle (Fig. 1) [51], and is related to the curvature tensor

by $C_u^u = \psi'/h$. We find from the definition of h and Eqs. (12)–(15) that

$$\partial_t h = [(v^u - q^u)h]' + v_n \psi'. \quad (16)$$

The significance of Eq. (16) for this work is as follows: From $h = |\partial_u \mathbf{X}|$, we see that $h(u, t)$ mediates via

$$s(u, t) = \int_0^u d\bar{u} h(\bar{u}, t) \quad (17)$$

a relationship between the fixed mesh coordinates u used to parameterize numerical solutions and the physical arc length $s(u, t)$ along the meridional outline [19]. Consequently, the numerical resolution of the physical surface directly depends on the dynamic properties of $h(u, t)$.

D. Scaling Eulerian-Lagrangian parameterization

For purely Eulerian ($q^u = v^u$) or Lagrangian ($q^u = 0$) parameterizations and without regular remeshing, the dynamics of $h(u, t)$ Eq. (16), and consequently the resolution of the physical surface, is dictated by the local surface flows \mathbf{v} and is therefore not under our direct control. To mitigate this lack of control, we choose a different approach in which the coordinate flow field q^u is determined by the constraint that $h(u, t) = h(t)$ has to remain spatially constant and thus becomes independent of local surface flows or deformations. If this can be achieved, the resulting parameterization will in general be neither Eulerian nor Lagrangian and Eq. (17) implies $L(t) = s(1, t) = h(t)$, where $L(t)$ is the total length of the meridional surface outline. Hence, $s(u, t) = L(t)u$ and $h(t)$ becomes a simple scaling factor that translates numerical mesh to physical arc length coordinates. We therefore will refer to the resulting parameterization as scaling Lagrangian-Eulerian (SLE) parameterization.

To determine the coordinate flow q^u of such an SLE, we impose $h' = 0$ in Eq. (16) and solve for q^u , which yields

$$q^u(u, t) = v^u(u, t) + \frac{1}{h(t)} \int_0^u d\bar{u} v_n(\bar{u}, t) \psi'(\bar{u}, t) + c_1(t) + c_2(t)u, \quad (18)$$

where $c_1(t), c_2(t)$ are integration constants and we included function arguments for clarity. The coordinate flow q^u given in Eq. (18) specifies the SLE parameterization. Integration constants are determined from suitable boundary conditions for q^u as

$$c_1 = q^u(0) - v^u(0) \quad (19)$$

$$c_2 = - (v^u - q^u)|_0^1 - \frac{1}{h} \int_0^1 du v_n \psi'. \quad (20)$$

We see from Eqs. (18)–(20) that this parameterization is only Eulerian ($q^u = v^u$) in the absence of deformations and if both boundary points satisfy $q^u = v^u$. Before discussing boundary conditions, it is instructive to plug the SLE coordinate

Parameterization	q^u	$\partial_t h$	References
Eulerian	v^u	$\psi' v_n$	[19]
Lagrangian	0	$(v^u h)' + \psi' v_n$	[12, 22]
SLE	s.t. $h' = 0$	dL/dt	This work

Table I. Comparison of parameterizations characterized by their coordinate flow q^u [see Eq. (2)]. The map $h(u, t)$ between fixed mesh coordinates u and physical arc length coordinates on the surface [see Eq. (16)] develops unpredictable flow- and shape-dependent inhomogeneities when purely Eulerian or Lagrangian parameterizations are used. The scaling Lagrangian-Eulerian (SLE) parameterization is independent of local flows v^u , deformations v_n and curvature ψ' and amounts to a simple linear map between mesh and arc length coordinates.

flow Eq. (18) back into the dynamics of the coordinate map, Eq. (16), which yields

$$\partial_t h = -[(c_1 + c_2 u)h]' \quad (21)$$

$$= (v^u - q^u) h|_0^1 + \int_0^1 du v_n \psi'. \quad (22)$$

The first equation self-consistently confirms that solutions with constant initial conditions $h = L_0$ remain spatially constant over time. As previously discussed, $h(t)$ is in this case equivalent to the total length $L(t)$ of the meridional outline (see Fig. 1). Using Eqs. (19), (20), Eq. (21) therefore explicitly shows how boundary flows (first term) and surface deformations (second term) contribute to changes of the meridional length $L(t)$.

The boundary conditions $q^u(u_b, t)$ for $u_b = 0, 1$ can in principle be chosen arbitrarily, but two natural choices are to treat a boundary point either as material point by setting $q^u(u_b, t) = 0$ or as Eulerian point by setting $q^u(u_b, t) = v^u(u_b, t)$. Both cases will be considered in the examples discussed below. As expected, Eq. (22) shows that Eulerian boundary points do not contribute to changes of the total meridional length.

III. MECHANICS OF DEFORMING ACTIVE FLUID SURFACES

A. Force and torque balance

The mechanical state of a curved surface is described by its tension and moment tensor, $\mathbf{T} = \mathbf{e}_i \otimes \mathbf{t}^i$ and $\mathbf{M} = \mathbf{e}_i \otimes \mathbf{m}^i$, where $\mathbf{t}^i = t^{ij} \mathbf{e}_j + t_n^i \mathbf{n}$ and $\mathbf{m}^i = m^{ij} \mathbf{e}_j + m_n^i \mathbf{n}$ are tension and moment vectors whose components describe in-plane (t^{ij}, m^{ij}) and out-of-plane or normal (t_n^i, m_n^i) contributions. In particular, for any line element of length ds on the surface with an in-plane unit vector $\boldsymbol{\nu} = \nu_i \mathbf{e}^i$ orthogonal to its vectors $\mathbf{F} = ds \boldsymbol{\nu} \cdot \mathbf{T} = ds \nu_i \mathbf{t}^i$ and $\boldsymbol{\tau} = ds \boldsymbol{\nu} \cdot \mathbf{M} = ds \nu_i \mathbf{m}^i$ yield the total force and the total torque, respectively, that acts on the line element. Force and torque balance equations for the

surface are given by [18]

$$\operatorname{div}(\mathbf{T}) = -\mathbf{f}^{\text{ext}} \quad (23)$$

$$\operatorname{div}(\mathbf{M}) = -\boldsymbol{\epsilon} : \mathbf{T}. \quad (24)$$

Here, $\operatorname{div}(\mathbf{T}) := \mathbf{e}^i \cdot \partial_i \mathbf{T}$ denotes the in-plane divergence of the tension tensor (analog for \mathbf{M}), $(\boldsymbol{\epsilon} : \mathbf{T})_\alpha = \epsilon_{\alpha\beta\gamma} T_{\beta\gamma}$, where $\epsilon_{\alpha\beta\gamma}$ is fully anti-symmetric Levi-Civita tensor (greek indices reference Cartesian components) and we do not include inertial forces or external torques. In the force balance Eq. (23), $\mathbf{f}^{\text{ext}} = f_i^{\text{ext}} \mathbf{e}^i + f_n^{\text{ext}} \mathbf{n}$ are external forces and we have neglected inertia, as we are interested in the typically overdamped dynamics of biological cells and tissues. In this work, we will consider external tangential friction forces

$$f_i^{\text{ext}} = -\Gamma v_i \quad (25)$$

with friction constant Γ . A general derivation of momentum conservation on curved surfaces described by an arbitrary Lagrangian-Eulerian parameterization is provided in the Appendix C 2 b. The torque balance Eq. (24) implies that inhomogeneous surface moments give rise to anti-symmetric components of the tension tensor \mathbf{T} , which correspond to contributions from anti-symmetric in-plane tensions t_{ij} and from normal forces t_n^i . In the absence of moments, $\mathbf{M} = 0$, \mathbf{T} must be symmetric, which is equivalent to a symmetric in-plane tension tensor t_{ij} and vanishing normal forces, $t_n^i = 0$. Center-of-mass velocities \mathbf{v} that drive the surface dynamics Eq. (1) will be determined by solving the force and moment balance equations (23) and (24). In the next step, we introduce the constitutive laws that relate tension \mathbf{T} and moments \mathbf{M} in the surface to its geometry and local center-of-mass velocity \mathbf{v} .

B. Constitutive laws

We will use our approach to study open and closed active fluid surface models that encapsulate essential physical features of membranes, the cell cortex and epithelial tissues. In anticipation of formulating a dissipation functional for such surfaces, we introduce constitutive laws by closely following their systematic construction within the framework of irreversible thermodynamics [18, 46]. We start by introducing the free energy density of the surface. The first contribution is given by the Helfrich free energy density [24]

$$f_H = \gamma_H + f_\kappa, \quad (26)$$

where γ_H denotes a passive isotropic surface tension and

$$f_\kappa = \frac{1}{2} \kappa (2H - C_0)^2 \quad (27)$$

includes a bending rigidity κ , the spontaneous curvature C_0 and $H = \operatorname{tr}(\mathbf{C})/2$ denotes the mean curvature. Second, we include the chemical free energy density $f_c(c_f, c_p)$ associated with surface concentrations c_f and c_p of chemical fuel and product species, respectively. In a biological system, these could be the reactant and product species involved

in ATP hydrolysis [52, 53]. The chemical potential difference $\Delta\mu = \mu_f - \mu_p$ with $\mu_n = \partial f_c / \partial c_n$ ($n = f, p$) provides the chemical energy to generate active stresses in the surface. The free energy of the whole surface Ω is then given by

$$F = \int_{\Omega} dA (f_H + f_c). \quad (28)$$

Such a free energy gives rise to well-defined, curvature-dependent equilibrium tensions and moments in the surface [18, 20] that are in the following denoted by \mathbf{T}_e and \mathbf{M}_e .

To introduce dissipative contributions, we use the symmetric strain rate tensor $S_{ij} = (v_{ij} + v_{ji})/2$, where $v_{ij} = \mathbf{e}_j \cdot (\partial_i \mathbf{v})$, and denote its traceless part by

$$\tilde{\mathbf{S}} = \mathbf{S} - \frac{1}{2} \operatorname{tr}(\mathbf{S}) \mathbf{G} \quad (29)$$

with $\mathbf{S} = S_{ij} \mathbf{e}^i \otimes \mathbf{e}^j$. Note also that $\operatorname{tr}(\mathbf{S}) = \operatorname{div}(\mathbf{v})$. We consider a dissipative contribution to the tension tensor given by

$$\mathbf{T}_d = 2\eta \tilde{\mathbf{S}} + \eta_b \operatorname{div}(\mathbf{v}) \mathbf{G} + \xi \Delta\mu \mathbf{G}, \quad (30)$$

where we have introduced shear viscosity and bulk viscosities η and η_b , respectively, as well as an active isotropic tension $\xi \Delta\mu$ that captures the conversion of chemical free energy into mechanical work. We do not consider dissipative moments, such that the tension and moment tensors used in this work are given by

$$\mathbf{T} = \mathbf{T}_e + \mathbf{T}_d \quad (31)$$

$$\mathbf{M} = \mathbf{M}_e. \quad (32)$$

From Onsager's symmetry relations [44–46], we expect from Eq. (30) an additional constitutive law for the thermodynamic variable conjugate to the chemical potential difference $\Delta\mu$. Introducing such a constitutive law in way that is compatible with the formulation of a dissipation functional involves a crucial subtlety that will be discussed in more detail in Section IV C.

IV. VARIATIONAL FORMULATION

For any given surface geometry and distribution of active tension $\sim \xi \Delta\mu$, force and torque balance Eqs. (23) and (24) with constitutive laws (31) and (32) determine in-plane flows and deformations \mathbf{v} . On an axisymmetric surface, these equations can be conveniently parameterized using the scaling Lagrangian-Eulerian parameterization introduced above. To characterise this active surface theory systematically, we have to explore the space of steady state geometries it gives rise to. To this end, we take inspiration from previous work on equilibrium membranes, whose phase diagrams of stationary equilibrium shapes have been extensively studied using a variational formulation [35]. By complementing the free energy Eq. (26) with suitable Lagrange multipliers, these formulations allow relaxing nonlinear geometric consistency re-

lations when minimizing the energy. This yields a system of differential equations that are together equivalent to the normal component of the force balance Eq. (23), while providing a more efficient path to identify stationary points of surface energies like Eq. (26). Here, we generalise this approach to out-of-equilibrium systems and replace the energy by a novel Rayleigh dissipation functional for active fluid surfaces. Specifically, the goal is to construct a functional \mathcal{R} whose stationary points defined by the variation

$$\frac{\delta \mathcal{R}}{\delta \mathbf{v}} = 0 \quad (33)$$

satisfy the force and torque balance Eqs. (23) and (24) for constitutive laws (31) and (32).

A. Free energy dynamics

The dissipation functional consists of contributions from both the equilibrium properties of the surface, as well as its dissipative properties. The former result from changes of the free energy given in Eq. (28), which follow from Eqs. (5) and (6) as

$$\begin{aligned} \frac{dF}{dt} = \int_{\Omega} dA \left(\frac{1}{\sqrt{g}} \partial_t (f_H \sqrt{g}) - r_p \Delta \mu \right. \\ \left. + \gamma_e \operatorname{div}(\mathbf{v}) + J_n^{\text{ext}} \right) + \oint_{\partial \Omega} f_H q^i \nu_i ds, \quad (34) \end{aligned}$$

where $r_p = -r_f$ denotes the rate at which the product species is produced due to fuel consumption, $\gamma_e = f_c - \mu_f c_f - \mu_p c_p$ is an equilibrium surface tension [18] and $J_n^{\text{ext}} = J_{n,f} \mu_f + J_{n,p} \mu_p$ denotes the in-flux of chemical free energy due to reactions with the surrounding [Appendix]. We assume that the flux J_n^{ext} is such that the chemical potential difference $\Delta \mu$ on the surface is maintained constant in space and time. Consequently, γ_e only renormalizes the isotropic surface tension γ_H and we denote the total passive tension by $\gamma = \gamma_H + \gamma_e$. The boundary term in Eq. (34), which is a consequence of the ALE parameterization, contributes to boundary conditions on open surfaces when performing variation of $\frac{dF}{dt}$. The Helfrich free energy dynamics in terms of an Eulerian parameterization has previously been derived in [39].

B. Entropy production

The dissipative part of the Rayleigh functional is defined by the entropy production in the surface. We denote the entropy production by Θ , which is given for an active isotropic fluid by [18, 42]

$$\Theta_{\text{int}} = \int dA (\mathbf{T}_d : \mathbf{S} + r_p \Delta \mu), \quad (35)$$

where each pair of conjugate thermodynamic variables contains one factor that is even ($\mathbf{T}_d, \Delta \mu$), and one that is odd (\mathbf{S}, r_p), under time-reversal. After choosing for each pair

which factor is treated as a thermodynamic flux and which is a thermodynamic force, all fluxes can be expanded near thermodynamic equilibrium in terms of forces following Onsager theory [44, 45]. This procedure yields constitutive laws such as Eq. (30), where η, η_b and ξ represent phenomenological Onsager coefficients [18, 42, 46]. Given the most commonly made choice of treating $\Delta \mu$ as thermodynamic force [52], as done in Eq. (30), a constitutive law for the thermodynamics flux r_p can be written as

$$r_p = \Lambda \Delta \mu - \xi \operatorname{div}(\mathbf{v}), \quad (36)$$

where we used $\mathbf{S} : \mathbf{G} = \operatorname{tr}(\mathbf{S}) = \operatorname{div}(\mathbf{v})$. The reappearance of the coefficient $-\xi$ is a consequence of the Onsager reciprocity relations: Because flux \mathbf{T}_d and force $\Delta \mu$ have the same time reversal-symmetry – the same is necessarily true for their cross-coupled conjugate partners $\operatorname{div}(\mathbf{v})$ and r_p – the coupling ξ is a reactive coefficient that must appear with opposite signs in the constitutive laws Eqs. (30) and (36) [46]. In the following, we will denote the entropy production Eq. (35) expressed in terms of constitutive laws Eqs. (30) and (36) as functional $\Theta_{\text{int}}(\mathbf{v}, \Delta \mu)$. Dissipative external forces, such as the effective friction introduced in Eq. (25), will additionally contribute the entropy production in the form

$$\Theta_{\text{ext}} = \int dA \mathbf{v} \cdot \mathbf{f}^{\text{ext}}. \quad (37)$$

C. Flux-force choice and dissipation functional

Reactive couplings, such as the Onsager coefficient ξ in Eqs. (30) and (36), do not contribute to the entropy production. This can easily be verified by plugging Eqs. (30) and (36) into the entropy production $\Theta_{\text{int}}(\mathbf{v}, \Delta \mu)$ given in Eq. (35). Thus, $\Theta_{\text{int}}(\mathbf{v}, \Delta \mu)$ cannot be used to construct the desired dissipation functional. Because only dissipative couplings remain in the entropy production the goal is then to formulate constitutive laws exclusively in terms of dissipative Onsager coefficients. Here, this can be realized by choosing – instead of $\Delta \mu$ – the chemical production rate r_p as the thermodynamic force. We write the resulting constitutive laws as

$$\hat{\mathbf{T}}_d = 2\eta \tilde{\mathbf{S}} + \left(\eta_b + \frac{\xi^2}{\Lambda} \right) \operatorname{div}(\mathbf{v}) \mathbf{G} + \frac{\xi}{\Lambda} r_p \mathbf{G} \quad (38)$$

$$\Delta \hat{\mu} = \frac{1}{\Lambda} r_p + \frac{\xi}{\Lambda} \operatorname{div}(\mathbf{v}), \quad (39)$$

where we have already parameterized the new Onsager coefficients that would appear such that Eqs. (38) and (39) are fully equivalent to the desired constitutive laws Eq. (30) and (36), i.e. $\hat{\mathbf{T}}_d = \mathbf{T}_d$ and $\Delta \hat{\mu} = \Delta \mu$. We denote the entropy production associated with constitutive laws Eqs. (38) and (39) as functional

$$\hat{\Theta}_{\text{int}}(\mathbf{v}, r_p) = \int dA \left(\hat{\mathbf{T}}_d : \mathbf{S} + r_p \Delta \hat{\mu} \right). \quad (40)$$

Note that, consistent with Onsager reciprocity relations, the Onsager coefficient ξ/Λ now appears as a dissipative term with the same sign in both constitutive laws Eqs. (38) and (39) and cross-couples flux-force pairs with opposite time-reversal signature. Consequently, it will contribute to the entropy production $\hat{\Theta}_{\text{int}}(\mathbf{v}, r_p)$. Furthermore, the constraint imposed by the second law of thermodynamics, $\hat{\Theta}_{\text{int}}(\mathbf{v}, r_p) \geq 0$, is fully compatible with the conditions for the Onsager coefficients η, η_b, ξ and Λ we obtain from $\Theta_{\text{int}}(\mathbf{v}, \Delta\mu) \geq 0$ [see Eqs. (30),(35),(36)]. Further, $\Theta_{\text{int}}(\mathbf{v}, \Delta\mu) \geq 0$ implies $\Lambda > 0$ and $\eta_b \geq 0$. Hence, $1/\Lambda > 0$ and $\eta_b + \xi^2/\Lambda \geq 0$, which is also independently required by the second law for $\hat{\Theta}_{\text{int}}(\mathbf{v}, r_p)$ and Onsager coefficients parameterized as in Eqs. (38) and (39).

It has been pointed out that the choice of thermodynamic fluxes and forces is essentially arbitrary [43, 54] and the physics described by the resulting constitutive laws will be the same for every choice. It is therefore not surprising that the transformation of the constitutive laws into Eqs. (38) and (39), based on a modified flux-force pair choice, exists. The fact that associated entropy productions take different forms for different flux-force choices and only some choices yield a suitable dissipation functional does also not contradict any physical principle: In contrast to, for example, energy minimization the minimization of dissipation invoked by Rayleigh functionals does not follow from any first physical principle and the existence of a suitable functional for any set of constitutive laws describing an out-of-equilibrium system is not guaranteed [43].

Taking everything together, the total dissipation rate used in this work is then given by

$$\mathcal{D}(\mathbf{v}, r_p) = \frac{1}{2} \left(\hat{\Theta}_{\text{int}} + \Theta_{\text{ext}} \right), \quad (41)$$

where $\hat{\Theta}_{\text{int}}(\mathbf{v}, r_p)$ denotes the entropy production given in Eq. (40) with $\hat{\mathbf{T}}_d$ and $\Delta\hat{\mu}$ given in Eqs. (38) and (39), respectively, as well as Θ_{ext} given in Eq. (25). Together with the contributions from the free energy given in Eq. (34), we arrive at the final Rayleigh dissipation functional

$$\mathcal{R}(\mathbf{v}, r_p) = \frac{dF}{dt} + \mathcal{D}. \quad (42)$$

We show in App. E that the variational equations (33) for $\mathcal{R}(\mathbf{v}, r_p)$ are equivalent to force and torque balance equations Eqs. (23), (24) with tension and moments Eqs. (31), (32), and the variation $\delta\mathcal{R}/\delta r_p = 0$ yields the remaining constitutive law Eq. (36).

D. Enforcing geometric relations and SLE parameterization via Lagrange multipliers

We demonstrate in this section that the equivalent formulation of force and torque balance equations in terms of the Rayleigh functional $\mathcal{R}(\mathbf{v}, r_p)$, Eq. (42), enables us to introduce Lagrange multipliers that dynamically impose nonlinear geometric relations and the SLE parameterization introduced above (Sec. IID). This will provide us with an approach that

can solve directly for stationary shapes of active isotropic fluid surfaces, and evolve their shape dynamics Eq. (1) in an implicit fashion. To discuss this in detail, we express Eq. (42) on an axisymmetric surface

$$\mathcal{R}(\mathbf{v}, r_p) = 2\pi \int_0^1 du R(\mathbf{v}, r_p) + 2\pi (f_H q^u r h)|_0^1, \quad (43)$$

where the form of the functional density $R(\mathbf{v}, r_p)$ follows from Eqs. (34), (37) and (40) and is provided in Appendix E 1. The functional density in Eq. (43) represents a functional $R[v^u, v^\phi, v_n, \partial_t r, \partial_t h, \partial_t \psi, q^u, r_p]$. For Eulerian or Lagrangian coordinates that fix the coordinate flow q^u , this density can be reduced to a functional $R[v^u, v^\phi, v_n, r_p]$, where the time derivatives $\partial_t r$, $\partial_t h$ and $\partial_t \psi$ have been expressed in terms of flow velocities according to Eqs. (14), (16) and (B9). While variations with respect to velocity components do recover the known force balance equations to determine \mathbf{v} (Appendix E), it disconnects from the shape dynamics in the embedding space and excludes explicit control over the mapping $h(u, t)$ between fixed mesh coordinates u and physical space [see Eq. (17)]. Using the SLE parameterization defined by Eq. (18) directly to fix the coordinate flow q^u also yields expressions for $\partial_t r$, $\partial_t h$ and $\partial_t \psi$ in terms of the flow velocities, but leads to impractical integro-differential equations when performing the variation.

To sidestep an explicit specification of the coordinate flow q^u entirely, while still imposing an SLE parameterization, we proceed as follows. From the shape dynamics of an axisymmetric surface, Eqs. (14) and (15), we find

$$v_n = \sin \psi \partial_t r + \cos \psi \partial_t z \quad (44)$$

$$q^u = v^u + h^{-1} (\sin \psi \partial_t z - \cos \psi \partial_t r). \quad (45)$$

Used those identities to eliminate v_n and q^u from the Rayleigh functional leads to remaining dependencies $R[v^u, v^\phi, \partial_t r, \partial_t z, \partial_t h, \partial_t \psi, r_p]$. Importantly, this substitution expresses two velocities, v_n and q^u , in terms of three other velocities $\partial_t r, \partial_t z$ and v^u . The relationship between $v_n, \partial_t r, \partial_t z$ and v^u becomes only unique once the coordinate flow q^u has been specified by a suitable constraint. Additionally, when computing variational equations it is desirable to treat the pair of variables $\partial_t r$ and $\partial_t z$ – that describe the shape dynamics in the embedding space – and the variable $\partial_t h$ – which can be used to implicitly enforce an SLE parameterization – as independent variables. However, the fields r, z and h are not independent, but related by geometric identities Eqs. (12) and (13) that additionally involve the tangent angle ψ . Therefore, we introduce Lagrange multipliers to impose Eqs. (12) and Eqs. (13), which enables us to treat $\partial_t r, \partial_t z, \partial_t h$ and $\partial_t \psi$ as independent when performing the variation. Finally, the SLE coordinate flow q^u given in Eq. (18) – more precisely a constraint for which the right-hand side of Eq. (45) corresponds to the SLE coordinate flow – has to be specified. To this end, we use that the requirement $h' = 0$ is sufficient to impose an SLE parameterization, as demonstrated in Sec. IID. All together, this leads to con-

Variation	Implied ODE
$\partial_t r$	$\alpha' = \dots$
$\partial_t z$	$\beta' = \dots$
$\partial_t \psi$	$\psi'' = \dots$
$\partial_t h$	$\zeta' = \dots$
$\partial_t \alpha$	$r' = \dots$
$\partial_t \beta$	$z' = \dots$
$\partial_t \zeta$	$h' = 0$
v^u	$\gamma'_H = \dots / (v^u)'' = \dots$
v^ϕ	$(v^\phi)'' = \dots$
γ_H	$(v^u)' = \dots / \text{n.a.}$

Table II. List of fields with respect to which the dissipation functional $\bar{\mathcal{R}} = \mathcal{R} + \mathcal{L}$, with \mathcal{R} and \mathcal{L} given in Eqs. (43) and (46) is varied and the differential equations implied by the corresponding variations. For an open incompressible surface variation w.r.t. the tension $\gamma_H(u)$ implies an additional ODE, that is not present in the compressible surface (n.a.).

straint terms

$$\mathcal{L} = 2\pi \int_0^1 du \partial_t [\alpha(r' - h \cos \psi) + \beta(z' + h \sin \psi) + \zeta h'] \quad (46)$$

that will be added to the Rayleigh dissipation functional Eq. (43), where α , β and ζ represent Lagrange multipliers that dynamically enforce the geometric relations Eqs. (12) and (13) and impose an SLE parameterization. The constrained Rayleigh dissipation functional $\bar{\mathcal{R}} = \mathcal{R} + \mathcal{L}$, with \mathcal{R} and \mathcal{L} given in Eqs. (43) and (46), respectively, has to be varied with respect to the independent fields $\Phi \in \{v^u, v^\phi, \partial_t r, \partial_t z, \partial_t h, \partial_t \psi, \partial_t \alpha, \partial_t \beta, \partial_t \zeta\}$. The structure of the system of ordinary differential equations (ODEs) obtained from

$$\frac{\delta \bar{\mathcal{R}}}{\delta \Phi} = 0 \quad (47)$$

is indicated in Tab. II, their explicit form is derived in App. E2. Taking everything together, this ODE system is for both incompressible and compressible fluid surfaces equivalent to 12 first order ODEs. It must therefore be complemented by 12 boundary conditions, which are listed in Table III and can be derived from the boundary terms of the functional variation Eq. (47) (App. F). In cases where closed surfaces with a conserved enclosed volume V_0 are considered (see Secs. VB 1, VB 2) this ODE system is complemented by an equation $V'(u) = \pi r^2 h \sin \psi$, which is by construction satisfied by the cumulative volume $V(u)$. The boundary condition $V(1) = V_0$ imposes the volume constraint, a second boundary condition, $V(0) = 0$ constraints a degree of freedom that determines the pressure difference p between the enclosed volume and the surrounding, which can directly be included as an external normal force $f_n^{\text{ext}} = p$.

Variation	Boundary conditions	
	Open surface	Closed surface
$\partial_t r$	$r(0) = 0, r(1) = R_b$	$r(0) = 0, r(1) = 0$
$\partial_t z$	$\beta(0) = 0, z(1) = 0$	$\beta(0) = 0, \beta(1) = 0$
$\partial_t \psi$	$\psi(0) = 0, \psi(1) = 0$	$\psi(0) = 0, \psi(1) = \pi$
$\partial_t h$	$\zeta(0) = 0, \zeta(1) = 0$	
v^u	$v^u(0) = 0, \gamma_H(1) = \gamma_0$	$v^u(0) = 0, v^u(1) = 0$
v^ϕ	$v^\phi(0) = 0, v^\phi(1) = 0$	

Table III. Boundary conditions used for open and closed surfaces that follow from boundary terms of the variation Eq. (47).

E. Implicit dynamics and direct computation of stationary states

1. Implicit time-stepping method for the surface dynamics

Having obtained a formulation of the surface dynamics in terms of the system of ODEs enables us now to conveniently - and robustly - perform dynamic simulations of deforming fluid surfaces. To this end, note that for the ODEs listed in Tab. II the right-hand side contains the time derivatives $\partial_t r, \partial_t z, \partial_t \psi$, which enter all equations by construction linearly. We can therefore design a fully implicit time integration scheme to evolve the surface shape by replacing

$$\begin{aligned} \partial_t r &= \frac{r(u, t) - r(u, t - \Delta t)}{\Delta t} \\ \partial_t z &= \frac{z(u, t) - z(u, t - \Delta t)}{\Delta t} \\ \partial_t \psi &= \frac{\psi(u, t) - \psi(u, t - \Delta t)}{\Delta t}, \end{aligned} \quad (48)$$

and using $r(u, t - \Delta t), z(u, t - \Delta t), \psi(u, t - \Delta t)$ from the previous time-step. Solutions $[r(u, t), z(u, t), \psi(u, t), v_u, v_\phi]$ of the ODE system derived from the variational formulation then directly correspond to surface geometries and flows at the next time point. Throughout this work, we use $\Delta t = 4 \times 10^{-4} \tau_\eta$ and $\Delta t = \times 10^{-3} \tau_\eta$ for simulations of open and closed surfaces, respectively. These iterative computations can be performed using standard boundary value solvers [55], as implemented for example in MATLAB.

2. Direct computation of stationary geometries and flows

While dynamic simulations are useful to qualitatively explore the parameter-dependence of a given model, they are not practical to systematically characterize the space of non-trivial stationary surface geometries and flows or the bifurcation structure of this space. However, with the formulation derived above, we can now directly compute steady state solutions by setting instead

$$\begin{aligned} \partial_t r &= 0 \\ \partial_t z &= v_0 \\ \partial_t \psi &= 0, \end{aligned} \quad (49)$$

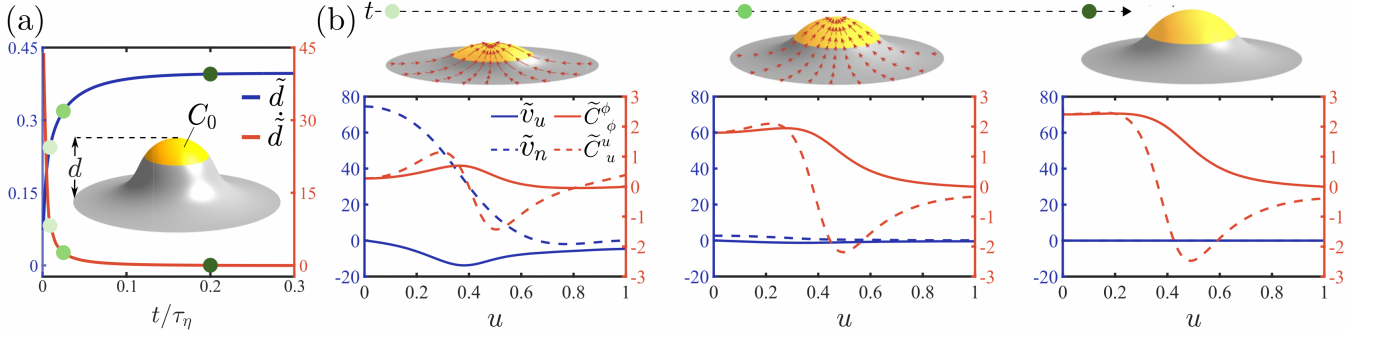


Figure 2. Dynamics of an open membrane with local spontaneous curvature coating [yellow patches, see Eq. (51)]. **(a)** Starting from a flat disk geometry, the membrane height $\tilde{d} = d/R_b$ (blue curve) grows in time t due to the coating ($\tau_\eta = \eta_s R_b^2/\kappa$, R_b is the fixed base radius). Red curve depicts growth speed. **(b)** Snapshots corresponding to (a) of membrane geometry at different times with tangential components of local center-of-mass flow velocities indicated by red arrows (top row). Bottom row shows flow velocity and curvature tensor components: Tangential velocity $\tilde{v}_u = \tilde{v}_u \tau_\eta / R_b$, normal velocity $\tilde{v}_n = v_n \tau_\eta / R_b$, azimuthal curvature $\tilde{C}_\phi^\phi = C_\phi^\phi R_b$ and meridional curvature $\tilde{C}_u^u = C_u^u R_b$. Last time point shows final stationary geometry ($v_n = 0$). Spontaneous curvature $\tilde{C}_0 = \tilde{C}_0 R_b$ is set $\tilde{C}_0 = 9$ [see Eq. (51)]. All other parameters are listed in Table IV.

Parameter	Value	Unit
κ	Bending rigidity	1 κ
η_s	Shear viscosity	1 η_s
R_b	Base radius	1 R_b
Γ	Friction	0.25 η_s/R_b^2
γ_0	Boundary tension	12.5 κR_b^{-2}
A_p	Coating area	2/25 $2\pi R_b^2$
σ_p	Coating profile sharpness	25 $1/(2\pi R_b^2)$
A_f	Area of external force	2/250 $2\pi R_b^2$
σ_f	Force profile sharpness	250 $1/(2\pi R_b^2)$

Table IV. Parameters used in open membrane examples shown in Figs. 2 and 3.

where v_0 is an additional parameter that represents a possible translational velocity of the surface along the symmetry axis. For open surfaces that are fixed at the base by boundary condition $z(1) = 0$, we have $v_0 = 0$ (see Tab. III). For closed surfaces that develop surface flows with a polar asymmetry and experience a friction Eq. (25), v_0 is an unknown parameter determined as part of the boundary value problem. In the latter case, the boundary condition $z(0) + z(1) = 0$ is added to fix a reference frame that is co-moving with the surface.

V. SURFACE DYNAMICS AND SHAPE SPACES

A. Formation of membrane protrusion via internal and external forces

To illustrate the flexibility of our method and its capacity to characterize emergent shape spaces, we first study deformations of an open circular patch of membrane in response to internal and external forces, and neglect contributions from the chemical free energy [consequently $\xi \Delta \mu = 0$ in Eq. (30)]. In all cases, we consider an incompressible membrane for which the isotropic tension γ_H in the Helfrich free energy Eq. (26) becomes a Lagrange multiplier that has to be dynamically

solved for (see Tab. II). The free energy dynamics Eq. (34) simplifies on the axisymmetric semi-open surface (Fig. 1a) to

$$\frac{dF}{dt} = 2\pi \int_0^1 du [\partial_t(rh f_\kappa) + rh \gamma_H \text{div}(\mathbf{v})] + 2\pi f_\kappa q^u hr|_{u=1}, \quad (50)$$

where we have used Eq. (B6), $\sqrt{g} = rh$ and $\nu_u = h$. The flow divergence $\text{div}(\mathbf{v})$ and bending rigidity contributions f_κ on axisymmetric surfaces are given in Eqs. (C18) and (D4), respectively.

1. Local spontaneous curvature

We first assign a finite spontaneous curvature ‘‘coating’’ to a sub-region of the membrane (Fig. 2a, inset), as can be induced by, for example, protein-patches on lipid membranes that play a role in clathrin-mediated endocytosis [36, 37, 56]. We assume this coating occupies the same material points at all the times. Starting from an initial profile [57]

$$C_0(u) = \frac{\tilde{C}_0}{2} (1 - \tanh\{\sigma_p [A(u) - A_p]\}), \quad (51)$$

where $A(u) = 2\pi \int_0^u du' rh$ denotes the cumulative surface area up to mesh coordinate u , the coating must therefore satisfy $\frac{d\tilde{C}_0}{dt} = 0$ or, explicitly,

$$\partial_t C_0 = -q^u \partial_u C_0, \quad (52)$$

where q^u is the coordinate flow imposed by the SLE. Starting from a flat geometry, surfaces with such a coating gradually bend and form protruding geometries (Fig. 2) as result of the spontaneous curvature coating. At first, the normal velocity v_n has its maxima at the center $u = 0$ and decays towards the base $u = 1$ where it is considered fixed by surrounding membrane. Gradients of spontaneous curvature generate inhomogeneous in-plane tension (App. D), which lead to in-plane flows v_u that accompany the protrusion process

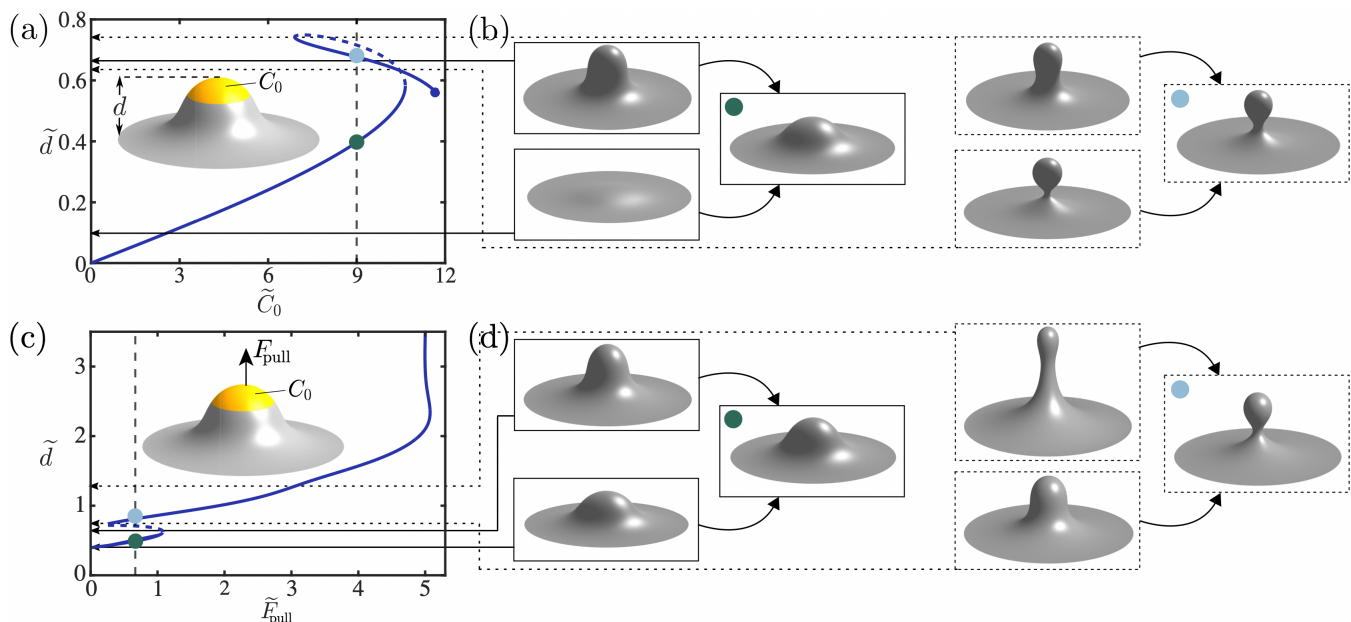


Figure 3. Nonlinear shape space analysis of open membranes. **(a)** Height $\tilde{d} = d/R_b$ of stationary surfaces as a function of the spontaneous curvature $\tilde{C}_0 = \hat{C}_0 R_b$ of the coated patch (yellow). This shape space trajectory is obtained by direct computation of stationary solutions as described in Sec. IV E and reveals stable (solid blue line) and unstable (dashed blue line) parts of the shape space trajectory. **(b)** Fixing the spontaneous curvature $\tilde{C}_0 = 9$, snapshots show different initial shapes and final stationary shapes [blue and green dot, also referenced in (a)] on the stationary shape space trajectory to which they relax. Stationary membrane geometries without (green dot) and with neck (blue dot) are discontinuously connected in shape space via the Gibbs loop in the (\tilde{C}_0, \tilde{d}) -space. **(c)** Stationary shape trajectory of membrane with spontaneous curvature coating ($\tilde{C}_0 = 9$) under application of varying external pulling force $\tilde{F}_{\text{pull}} = F_{\text{pull}} R_b / \kappa$ [see Eq. (53)]. At finite force the Gibbs loop from (a) becomes untangled, but a degeneracy of stable stationary shapes at fixed \tilde{F}_{pull} remains. Minimal force \tilde{F}_{pull} needed to reach a certain membrane height saturates at $\tilde{F}_{\text{pull}} \approx 5$ and membrane tubes are being pulled [34]. **(d)** Snapshots show initial shapes and stationary points on the shape space trajectory to which they relax when a fixed pulling force $\tilde{F}_{\text{pull}} = 0.7$ is applied. All other parameters are listed in Table IV.

(red arrows in Fig. 2b). Growth eventually saturates, leading to a non-trivial stationary membrane geometry and vanishing center-of-mass flows (Fig. 2b, right).

We now characterize the space of emergent stationary geometries as function of the local spontaneous curvature $\tilde{C}_0 = \hat{C}_0 R_b$ systematically. The corresponding trajectories of stationary geometries are obtained by direct computation as described in Sec. IV E. Interestingly, this analysis reveals a non-monotonic and non-bijective behaviour of the stationary membrane height d as a function of \tilde{C}_0 (Fig. 3a). Consequently, for an intermediate range of local spontaneous curvature, three distinct stationary geometries are associated with a given spontaneous curvature imposed by the coating. A subsequent control in which the identified stationary geometries are perturbed and used as initial conditions in dynamic simulations enables the identification of two stable and one unstable branch (solid and dashed lines, respectively, in Fig. 3a) in the degenerate parameter region. Such a degeneracy of membrane shapes was previously discussed in the context of a snap-through instability [36]. Fixing as an example $\tilde{C}_0 = 9$ (black vertical dashed line in Fig. 7a) and considering different geometries as initial conditions the convergence to stationary surface geometries on intersection of stable branches with $\tilde{C}_0 = 9$ is illustrated in Fig. 3b. In the degenerate shape space region the two stable branches correspond to protrusion with and without a neck – a region with negative Gaussian cur-

vature (blue and green dots in Figs. 3a,b, respectively). Our analysis therefore reveals, consistent with previous observations [36, 56] that the transition between these two types of geometries corresponds to a first-order transition.

2. Pulling forces

We next study membrane deformations under an external force density $\mathbf{f}^{\text{ext}} = f_z^{\text{ext}} \mathbf{e}_z$, while maintaining the spontaneous curvature coating. The external force density amounts to a total applied pulling force $F_{\text{pull}} = \int dA f_z^{\text{ext}}$. The impact of turgor pressure on such a configuration was previously discussed [56]. Here, we are interested in understanding how the pulling force interacts with the first-order transition we have identified above. We parameterize the pulling force density by a sigmoidal function of the form

$$f_z^{\text{ext}}(u) = \frac{f_0}{2} (1 - \tanh \{ \sigma_f [A(u) - A_f] \}). \quad (53)$$

In Eq. (53), f_0 is the magnitude of the applied force density, A_f denotes the approximate total area of the region to which it is applied and σ_f is the inverse width of the transition between forced and unforced membrane region. This problem has been discussed in the absence of a spontaneous curva-

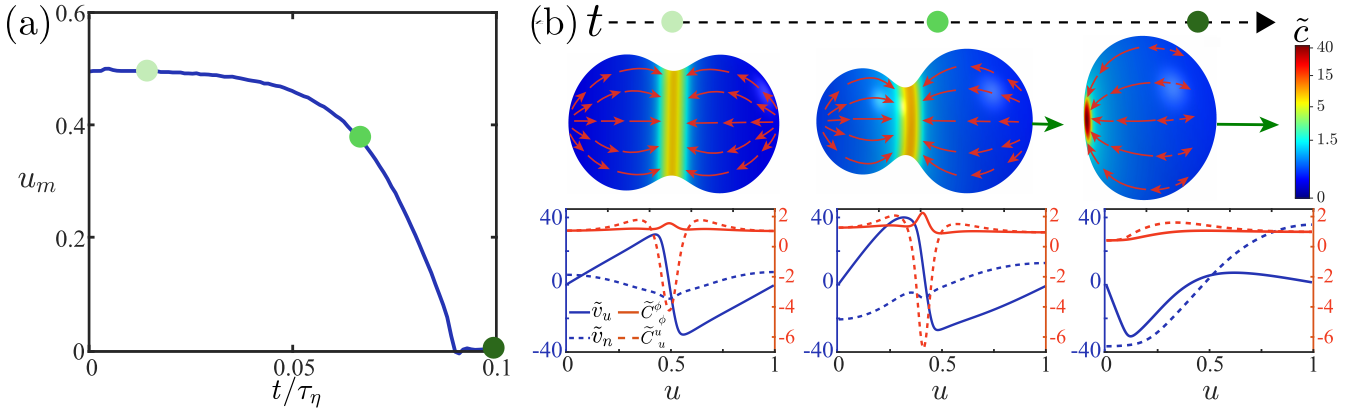


Figure 4. Self-organisation dynamics, contractile ring slipping and propagation of a closed active isotropic fluid surface. **(a)** Mesh coordinate u_m of maximal stress-regulator concentration over time ($\tau_\eta = \eta_0 R_0^2/\kappa$) when initiating a centered contractile ring profile $c(u)_{t=0} = \hat{c}_0[0.2 + 2 \exp(-(u - 1/2)^2/w^2)]$. The contractile ring remains initially centered but eventually slips to one of the poles (here the pole at $u = 0$). **(b)** Snapshots of surface shapes with surface flow velocities indicated by red arrows, colour code indicates stress regulator concentration $\tilde{c} = c/\hat{c}_0$. Last snapshot shows final surface geometry. Velocity ($\tilde{v}_u = \tilde{v}_u \tau_\eta/R_0$, $\tilde{v}_n = \tilde{v}_n \tau_\eta/R_0$) and curvature ($\tilde{C}_\phi^\phi = C_\phi^\phi R_0$, $\tilde{C}_u^u = C_u^u R_0$) component profiles at corresponding time points are shown in the bottom row. The polar symmetry breaking leads to directed surface flows as previously found [19, 20]. Here, due to friction with the surrounding [see Eq. (25)], this emergent mechano-chemical polar pattern leads to a continuous translation of the final stationary shape akin to surface-driven microswimmers [58–60]. Relative swimmer speeds are indicated by green arrows. Note, surface flow velocities indicated by red arrows in the snapshots and velocity components plotted are in the lab frame. As a result, $v_n \neq 0$ in the last snapshot, even though the surface geometry is stationary. Values of other parameters are listed in Table V.

ture coating in [34], where a distinct first-order transition was identified after which membrane protrusions become tubular and keep growing at constant force. While this phenomenology is recovered in Fig. 3c at $\tilde{F}_{\text{pull}} \approx 5$, we find an additional first-order transition at smaller pulling forces ($\tilde{F} \approx 1$) when the spontaneous curvature coating is present. Analyzing the stability of the corresponding stationary surfaces as before, stable and unstable regions of the shape trajectory (solid and dashed blue lines in Fig. 3c, respectively) can be identified. Exemplary transitions under fixed pulling force ($\tilde{F}_{\text{pull}} = 0.7$, black vertical dashed line in Fig. 3c) between different initial conditions and corresponding stationary states are shown in Fig. 3d. The reappearance of protruded stationary surfaces without and with neck along separated stable branches (green and blue dots in Figs. 3c,d) confirms that the associated first-order transition at smaller pulling forces is indeed a remaining signature of the transition illustrated in Figs. 3a,b.

B. Spontaneous polarization, propagation and guided division of closed active fluid surfaces

We now include chemically regulated active stresses $\sim \xi \Delta \mu$ as introduced in the dissipative tension tensor Eq. (30) and investigate self-organised deformations and emergent shape spaces of closed active fluid surface. Following previous work [19, 20, 61, 62], we consider a concentration field c that represents force-generating molecules and satisfies a continuity equation of the general form Eq. (6). We use a diffusive flux $j_i = -D \partial_i c$ with diffusion constant D and a normal flux $J_n = -k(c - c_0)$ describing the exchange of molecules with the surrounding at a rate k to maintain a reference concentration c_0 on the surface. The dynamics of stress regulators then

reads

$$\frac{dc}{dt} + \text{div}(\mathbf{v})c = D\Delta c - k(c - c_0), \quad (54)$$

where $\frac{dc}{dt} = \partial_t c + q^i \partial_i c$, Δ is the Laplace-Beltrami operator on the curved surface and an expression for $\text{div}(\mathbf{v})$ is provided in Eq. (7). We will explore a general scenario in which the reference concentration c_0 profile can correspond to a centered contractile ring, i.e.

$$c_0(u) = \hat{c}_0 \left[1 + \Delta_c \exp\left(-\frac{(u - \frac{1}{2})^2}{w^2}\right) \right]. \quad (55)$$

The cases $\Delta_c = 0$ and $\Delta_c > 0$ will be discussed in Secs. VB 1 and VB 2, respectively. In the context of a cellular cortex, an externally imposed profile of the form Eq. (55) can be the result of biochemical signaling originating from the spindle [63, 64].

We assume the isotropic stress produced by the stress-regulator depends on the concentration according to [19]

$$\xi \Delta \mu(c) = (\xi \Delta \mu)_0 \frac{c^2}{c^2 + c_s^2}, \quad (56)$$

where c_s denotes the saturation density.

1. Polarization and propagation

We first discuss the case $\Delta_c = 0$ in Eq. (55) for which the reference concentration $c_0 = \hat{c}_0$ in Eq. (54) is constant. Using this model, it has been shown in the absence of friction that a

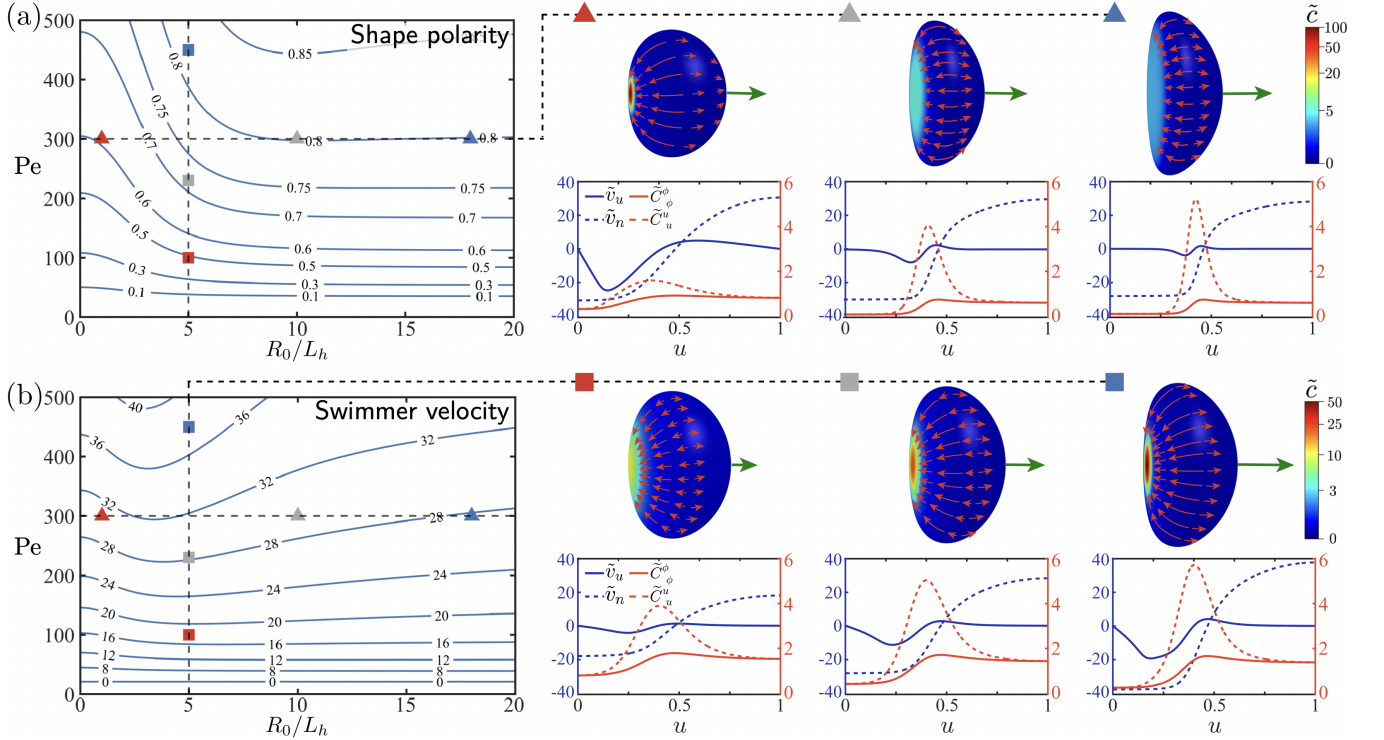


Figure 5. Shape space characterization of polarized stationary surfaces. **(a)** Contour plot of surface shape polarity $P = 1 - H(0)/H(1)$, where $H(u) = C_k^k/2$ is the mean curvature, as function of Péclet number $Pe = (\xi\Delta\mu)_0 R_0^2 / (D\eta_b)$ and inverse relative hydrodynamic length R_0/L_h , where $L_h = \sqrt{\eta_b/\Gamma}$. Contours were obtained by direct computation of nonlinear stationary surface solutions using the approach described in Sec. IV E. At fixed Péclet number $Pe = 300$, a decreasing hydrodynamic length increases the geometric shape polarity (triangles) until it saturates. Exemplary stationary solutions with tangential flow velocities (red arrows), surface propagation speed (green arrows) and concentration patterns (color-code) are depicted on the right. **(b)** Contour plot of propagation speed of polarized active surfaces. Increasing Péclet number increases swimmer speed as a result of increased tangential flow velocities. Exemplary stationary solutions are depicted on the right. Analysis for turnover rate $k\tau_\eta = 9$, all other parameters are listed in Table V.

Parameter	Value	Unit
κ	Bending rigidity	1 κ
η_b	Bulk viscosity	1 η_b
η_s	Shear viscosity	1 η_b
R_0	Spherical radius	1 R_0
Γ	Friction	0.09 η_b/R_0^2
\hat{c}_0	Steady state concentration	1 \hat{c}_0
$\gamma = \gamma_H + \gamma_e$	Passive tension	9 κR_0^{-2}
D	Diffusion constant	1 R_0^2/τ_η
k	Turnover rate	45 τ_η^{-1}
$(\xi\Delta\mu)_0$	Active contractility	450 $D\eta_b/R_0^2$
c_s	Saturation concentration	10 \hat{c}_0
w	Preferred concentration profile width	0.02 1

Table V. Parameters used in closed active fluid surface examples shown in Figs. 4–7. Characteristic length scale R_0 is related to the enclosed conserved volume by $V = 4\pi R_0^3/3$.

spherical surface with uniform distribution of stress-regulator undergoes a mechano-chemical shape instability above a critical active stress $(\xi\Delta\mu)_0$ [19]. As a result of this instability, chemical patterns and surface geometry break symmetry

along the z -axis, eventually reaching a steady state that is polarized. This polarization dynamics still occurs in the presence of friction, and even if alternative patterns are imposed initially, as we demonstrate in Fig. 4. There, we use a centered ($u = 1/2$) ring-like concentration pattern as initial condition and follow the position of the concentration maximum over time (Fig. 4a). While such ring patterns remain initially centered, they eventually move towards one of the surface's poles ($u = 0, 1$). Surface snapshots of this process and quantitative information on curvature and flow speeds are provided in Fig. 4b. The ring does initially lead to an ingress before it slips, consistent with geometric minimal models of cell division [16, 65], and a polar concentration pattern and surface geometry remains. Due to the friction, and in the presence of a polarized surface state, surfaces will propagate in the lab frame. Green arrows in Fig. 4 indicate the relative magnitude of propagation speeds as ring-slipping occurs, which shows indeed a clear correlation between polarization and propagation speed. The physics of this mode of propagation is closely related to squirmer models [66], droplets driven by Marangoni flows [59, 67] and can also be observed when embedding active surfaces into a passive fluid [68].

We now want to exploit the capacity of our functional formulation to directly compute nonlinear stationary states in or-

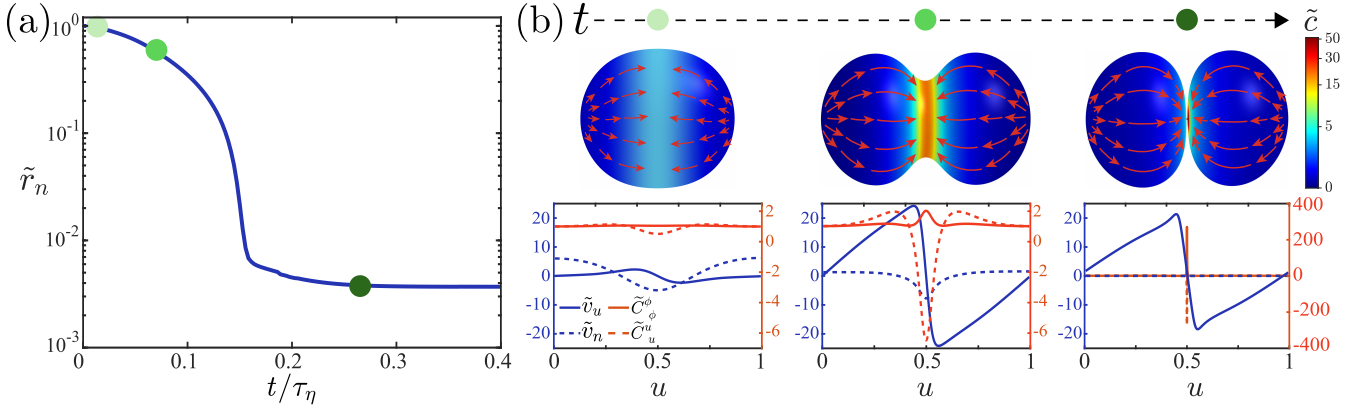


Figure 6. Dynamics of guided furrow formation and emergence of extreme localized curvature. **(a)** Evolution of the neck radius $\tilde{r}_n = r_n/R_0$ with $r_n := r|_{u=1/2}$ from an initially spherical surface ($\tilde{r}_n = 1$) and homogeneous concentration ($c(u)_{t=0} = \hat{c}_0$), where force generator dynamics Eq. (54) includes an inhomogeneous pattern of preferred concentration $c_0(u)$ [Eq. (55)]. The magnitude of the inhomogeneity is set to $\Delta_c = 4$. $\tau_\eta = \eta_b R_0^2/\kappa$. A finite neck radius remains due to bending rigidity κ . **(b)** Snapshots of surface shapes with surface flow velocities indicated by red arrows, colour code indicates stress-regulator concentration $\tilde{c} = c/\hat{c}_0$. Bottom panels show velocity ($\tilde{v}_u = v_u\tau_\eta/R_0$, $\tilde{v}_n = v_n\tau_\eta/R_0$) and curvature tensor ($\tilde{C}_\phi^\phi = C_\phi^\phi R_0$, $\tilde{C}_u^u = C_u^u R_0$) component profiles. Note the large localized curvature values in the neck region $u = 1/2$ that our approach can robustly simulate. All remaining parameter values are listed in Table V .

der to characterize the relationship between surface geometry, propagation velocity and key parameters of active surface swimmers in more detail. In particular, we will focus on the interplay of the hydrodynamic length $L_h = \sqrt{\eta_b/\Gamma}$ relative to system size R_0 , and the Péclet number $\text{Pe} = \xi\Delta\mu R_0^2/(D\eta_b)$ that characterizes the strength of active contractility [61]. To this end, we perform direct computations of stationary geometries and flows on a 250×250 grid in the (Pe, R_0, L_h) space and evaluate a heuristic measure of geometric polarity, $P = 1 - H(u = 0)/H(u = 1)$ (Fig. 7a), where H is the mean curvature, and the propagation speed (Fig. 7b). The contour plots generated from this analysis provide insights into how the relative hydrodynamic length L_h and the activity quantified by Pe control surface shape and propagation speed. Note, that for $\text{Pe} < \text{Pe}^*$, where $\text{Pe}^* = 2(kR_0^2/D + 2)$ is a known mechano-chemical instability threshold [19], stress regulator patterns do not spontaneously form. Consequently, the surface remains spherical ($P = 0$) and at rest ($v_0 = 0$) in this regime. For $\text{Pe} > \text{Pe}^*$ and in the presence of strong hydrodynamic screening (R_0/L_h large), it is dominantly the Péclet number Pe that affects shape polarity and propagation speed, which both increase with increasing activity. This impact of the Péclet number was expected, given that it quantifies the strength of contractility and therefore essentially the magnitude of tangential flows that move the surface forward (see quantified flow fields in Fig. 5b). Interestingly, in a regime where $R_0/L_h \approx 1$, which corresponds to a regime where hydrodynamic screening changes from being irrelevant ($R_0/L_h < 1$) to being relevant ($R_0/L_h > 1$), changes of the hydrodynamic length have a strong impact on the surface polarity, while still having relatively little impact on the propagation velocity. Exemplary stationary geometries, flows and stress regulator patterns (snapshots in Fig. 7a) suggest an explanation for this phenomenology. Strong hydrodynamic screening for large R_0/L_h leads to stationary stress regulator patterns that put a large part of the surface under high

tension. As a result, the surface is significantly flattened on one side and shape polarity increases. The lack of change in propagation velocities appears to be the result of two counteracting factors: Due to the broad contractility pattern tangential flows localize strongly to the equatorial region of the surface ($u \approx 1/2$) when R_0/L_h is increased. This leads to a more effective propulsion that compensates for the fact that surface flow magnitudes are strongly reduced and as a result overall surface propagation speeds remains roughly constant.

2. Guided division

In this last section, we characterise the impact of an inhomogeneous, preferred stress-regulator profile – Eq. (55) with $\Delta_c > 0$. A representative example of the shape dynamics is depicted in Fig. 6. For sufficiently large contractility ($\xi\Delta\mu$) and turnover rate k a contractile ring forms and persists, leading to an almost complete ingression of the surface (neck radius $r_n := r(u = 1/2)$ over time shown in Fig. 6a. A finite-sized neck as approached in this case will always exist due to bending rigidity κ . Snapshots of the corresponding dynamics are shown in Fig. 6b together with quantitative information about surface flows and curvature. The final snapshot reveals large localized curvature values ($|R_0 C_u^u| > 200$) in the neck region and highlights the extreme geometric regimes our approach can robustly capture.

To gain a deeper understanding of the overall space of emerging surface geometries, we next directly compute stationary geometries and flows on a dense grid in the (Δ_c, Pe) -space (Fig. 7a) using the approach described in Sec. IV E 2. The time series shown in Fig. 6 was obtained for parameters indicated by the green dot in 7a. This parameter sweep reveals three regimes: i) When either the contractility (quantified by the Péclet number Pe) or the inhomogeneity magnitude Δ_c are small final stationary surfaces are ellipsoidal with positive

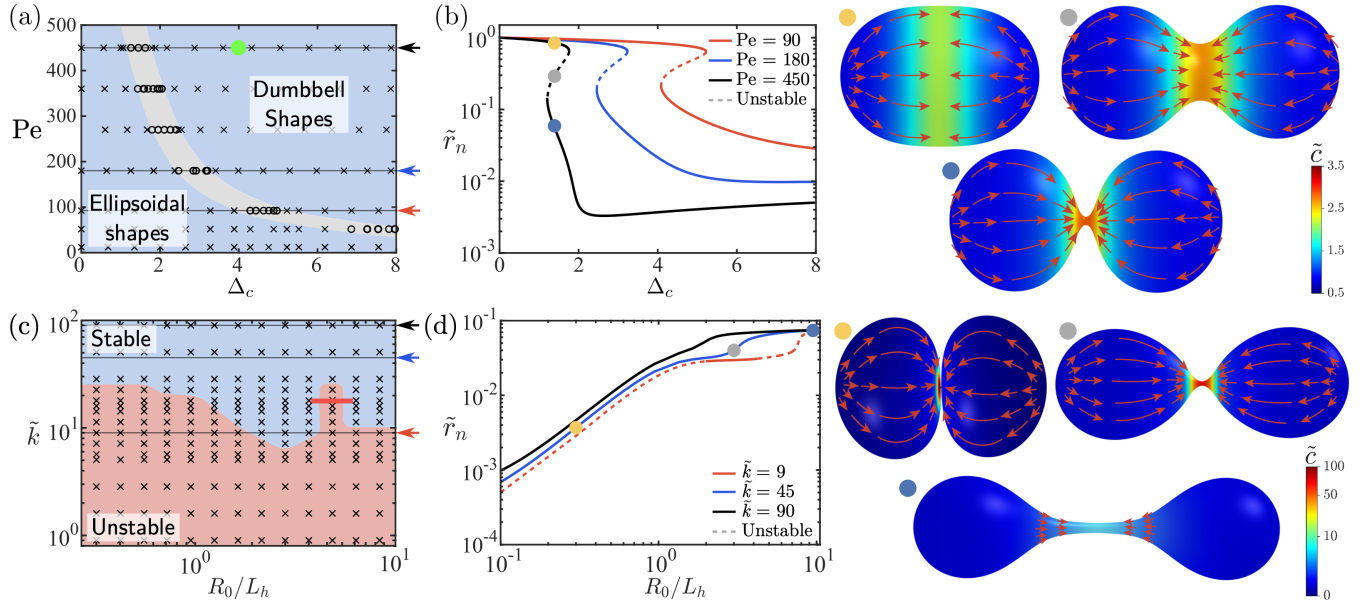


Figure 7. Shape space analysis of guided furrow model (see Fig. 6). **(a)** Phase space of stationary surface geometries and flows – as function of Péclet number and magnitude Δ_c of contractile ring pattern [see Eq. (55)] – obtained by direct computation of nonlinear stationary surface solutions using the approach described in Sec. IV E. Black symbols indicate complementary dynamic simulations to test stability of the stationary states. Crosses correspond to regions with unique attractors: dumbbell-shaped and ellipsoidal surfaces. Black circles identify parameter regions with multiple attractors. Green dot depicts parameters used in Fig. 6. **(b)** 1D slices through phase space in (a) show stable (solid lines) and unstable (dashed lines) branches and reveals a first-order transition between stationary ellipsoidal and dumbbell shapes. Exemplary stationary solutions in the degenerate part of the shape space [gray region in (a)] are shown on the right. Red arrows indicate surface flows, colour code indicates stress generator concentration $\tilde{c} = c/\hat{c}_0$. **(c)** Stability diagram of symmetrically ingressed stationary surfaces ($\Delta_c = 4$, $Pe = 450$ – green dot in a). Black crosses depict parameters for which dynamic simulations were performed to test the mechanical surface stability (red: unstable, blue: stable). The instability “finger” (passed through by red line) corresponds to a pitchfork bifurcation with control parameter R_0/L_h in which two stable branches with slightly asymmetrically placed rings emerge (and disappear). **(d)** Slices through phase space in (c) show stable (solid lines) and unstable (dashed lines) branches for different turnover rates. Yellow dot corresponds to parameters used in Fig. 6. All other parameters used for this analysis are listed in Table V. Exemplary stationary solutions along the fully stable branch with $k = 45$ are shown on the right.

Gaussian curvature everywhere. ii) When either the contractility or the inhomogeneity magnitude are sufficiently large a neck with locally negative Gaussian curvature forms. iii) In an intermediate regime both ellipsoidal and dumbbell-shaped stationary surfaces can be found for fixed Pe and Δ_c . Parameter regions corresponding to i), ii) and parameter regions corresponding to iii) are colored in Fig. 7a in blue and gray, respectively. In the non-degenerate regions independent dynamic simulations of perturbed stationary surfaces suggest all surfaces are mechanically stable.

Figure 7b traces stationary shape trajectories in terms of neck radii for different fixed Péclet numbers (indicated additionally by black lines in Fig. 7a). In addition to the stable regimes just described (solid lines, unique solution for given Δ_c) this analysis reveals overhangs that characterize a first-order shape transition. In this parameter regime (gray region in Fig. 7a) three stationary solutions exist for both Pe and Δ_c fixed: two on stable branches and one on an unstable branch. Exemplary surface geometries and flows from those three branches are shown on the right of Fig. 7b, confirming the first-order transition occurs between surface geometries without (yellow dot) and with (blue dot) neck.

Finally, we want to challenge the stability of the symmetrically

geometries found in the previous analysis by modifying the turnover rate k and investigate – motivated by the observation in Fig. 5 – if and how hydrodynamic screening imposed by the hydrodynamic length $L_h = \sqrt{\eta_b/\Gamma}$ affects stationary surface geometries in the presence of inhomogeneous concentration regulation $\Delta_c > 0$. Fixing $Pe = 450$ and $\Delta_c = 4$, direct computation of symmetrically ingressed stationary geometries and flows in the $(k, R_0/L_h)$ -space leads to the stability diagram shown in Fig. 7c. We find that the turnover rate k has to be larger than a certain threshold for symmetrically ingressed stationary surfaces to be mechanically stable. This can be understood intuitively. We know from the shape space analysis for $\Delta_c = 0$ (Figs. 4 and 5) that centered contractile rings are generally unstable and contractility patterns exhibit an inherent propensity to polarize the surface instead. This ring-slipping will have a certain time-scale associated with it, which the rate k in Eq. (54) has to compete against when turning over and restoring the centered preferred stress-regulator concentration profile. The instability threshold as function of the inverse hydrodynamic length R_0/L_h forms a rugged, non-monotonic interface in the $(k, R_0/L_h)$ -space. This interface includes a “finger” region in which symmetrically ingressed stationary surfaces become unstable (and stable again) only by

changing R_0/L_h (red line in Fig. 7c). A careful analysis of all stationary branches in this regime reveals the occurrence of an additional supercritical pitchfork bifurcation at which a symmetric surface becomes unstable, while two stable branches with a slightly asymmetrically placed ingression extrude (and merge again).

Shape trajectories in terms of their neck radius for different fixed turnover rates are shown in Fig. 7d, together with snapshots of stationary surfaces along a fully stable branch and for different hydrodynamic lengths. Analog to the results from Fig. 3a, changes in hydrodynamic length have the most significant impact around $R_0/L_h \approx 1$, when it changes from being irrelevant to becoming relevant on the surface given the characteristic domain size $\sim R_0$. Emerging geometries change from sharply divided surfaces to more lengthy dumbbell geometries by the same mechanism discovered in Sec. VB 1: Hydrodynamic screening leads for $R_0/L_h < 1$ to more spread out steady state patterns of stress-regulator. This results in a broader surface region in which contractile tension is high and consequently the neck region expands (green dot, Fig. 7d).

VI. CONCLUSION

The focus of this work was on isotropic active stresses, it is straightforward to generalize this framework to analyze the large variety of unexplored constitutive laws for active surfaces with different broken symmetries that have recently been derived [42]. In order to exploit the symmetries imposed by Onsager relations in such a generalization, one has to consider

constitutive laws that are linear in the thermodynamic forces. The algebraic properties of the coupling matrix that contains the phenomenological coefficients is in this case always such that equivalent constitutive laws can be formulated that contain exclusively dissipative couplings. While this may sound restrictive, it is an acceptable limitation given the remarkably broad success of such linear constitutive laws in quantitatively explaining biological processes.

Many aspects of the approach formulated here benefit from the simplifying restriction to axisymmetric surfaces. It will be interesting to investigate which of these insights can potentially be carried over to surfaces without pre-imposed symmetry. While the dissipation functional is itself agnostic to this question, one may ask how the analog of the scaling Lagrangian-Eulerian parameterization could look like on a general surface. This could be guided by the aim to minimize the distortion in the map from a reference space to the deforming surface. While on the axisymmetric surface this corresponds to the elimination of inhomogeneous parametric stretching along the meridional outline, one would also have to minimize the effects of shearing and twisting in the parameterization of a general two-dimensional surface.

The application of our framework to two simple minimal models of self-organising deforming fluid surfaces has highlighted the advantages of a systematic analysis of stationary shape spaces. Studying alternative constitutive laws for surfaces with broken symmetries therefore promises to reveal, and will enable us to systematically classify, a rich phenomenology in active surfaces with relevance for our understanding of the emergence of shape during biological development.

-
- [1] M. Kaksonen and A. Roux, *Nat. Rev. Mol. Cell Biol.* **19**, 313 (2018).
 - [2] R. Jahn and T. C. Südhof, *Annu. Rev. Biochem.* **68**, 863 (1999).
 - [3] L.-G. Wu, E. Hamid, W. Shin, and H.-C. Chiang, *Annu. Rev. Physiol.* **76**, 301 (2014).
 - [4] R. Dimova, S. Aranda, N. Bezlyepkina, V. Nikolov, K. A. Riske, and R. Lipowsky, *J. Phys. Condens. Matter* **18**, S1151 (2006).
 - [5] B. Alberts, D. Bray, J. Lewis, M. Raff, K. Roberts, and J. Watson, *Molecular Biology of the Cell*, 4th ed. (Garland, 2002).
 - [6] R. Phillips, J. Kondev, J. Theriot, and H. Garcia, *Physical biology of the cell* (Garland Science, 2012).
 - [7] G. Salbreux, G. Charras, and E. Paluch, *Trends Cell Biol.* **22**, 536 (2012).
 - [8] D. Bray and J. White, *Science* **239**, 883 (1988).
 - [9] M. Mayer, M. Depken, J. S. Bois, F. Jülicher, and S. W. Grill, *Nature* **467**, 617 (2010).
 - [10] T. Lecuit and P.-F. Lenne, *Nat. Rev. Mol. Cell Biol.* **8**, 633 (2007).
 - [11] P. Chugh, A. G. Clark, M. B. Smith, D. A. D. Cassani, K. Dierkes, A. Ragab, P. P. Roux, G. Charras, G. Salbreux, and E. K. Paluch, *Nat. Cell Biol.* **19**, 689 (2017).
 - [12] H. Turlier, B. Audoly, J. Prost, and J.-F. Joanny, *Biophys. J.* **106**, 114 (2014).
 - [13] A. C. Martin, M. Gelbart, R. Fernandez-Gonzalez, M. Kaschube, and E. F. Wieschaus, *J. Cell Biol.* **188**, 735 (2010).
 - [14] C.-P. Heisenberg and Y. Bellaïche, *Cell* **153**, 948 (2013).
 - [15] J. Ranft, M. Basan, J. Elgeti, J.-F. Joanny, J. Prost, and F. Jülicher, *Proc. Natl. Acad. Sci. U.S.A.* **107**, 20863 (2010).
 - [16] A. Daeden, A. Mietke, E. Derivery, C. Seum, F. Jülicher, and M. Gonzalez-Gaitan, *Nat. Cell Biol.* **25**, 235 (2023).
 - [17] M. Denk-Lobnig, J. F. Totz, N. C. Heer, J. Dunkel, and A. C. Martin, *Development* **148**, dev199232 (2021).
 - [18] G. Salbreux and F. Jülicher, *Phys. Rev. E* **96**, 032404 (2017).
 - [19] A. Mietke, F. Jülicher, and I. F. Sbalzarini, *Proc. Natl. Acad. Sci. U.S.A.* **116**, 29 (2019).
 - [20] A. Mietke, V. Jemseena, K. V. Kumar, I. F. Sbalzarini, and F. Jülicher, *Phys. Rev. Lett.* **123**, 188101 (2019).
 - [21] A. Torres-Sánchez, M. K. Winter, and G. Salbreux, *PLOS Comp. Biol.* **18**, e1010762 (2022).
 - [22] D. Khoromskaia and G. Salbreux, *eLife* **12**, e75878 (2023).
 - [23] P. B. Canham, *J. Theor. Biol.* **26**, 61 (1970).
 - [24] W. Helfrich, *Zeitschrift für Naturforschung C* **28**, 693 (1973).
 - [25] E. A. Evans, *Biophys. J.* **14**, 923 (1974).
 - [26] O.-Y. Zhong-can and W. Helfrich, *Phys. Rev. Lett.* **59**, 2486 (1987).
 - [27] O.-Y. Zhong-can and W. Helfrich, *Phys. Rev. A* **39**, 5280 (1989).
 - [28] R. Lipowsky, *Nature* **349**, 475 (1991).
 - [29] U. Seifert, K. Berndl, and R. Lipowsky, *Phys. Rev. A* **44**, 1182 (1991).

- [30] H. Jian-Guo and O.-Y. Zhong-Can, Phys. Rev. E **47**, 461 (1993).
- [31] F. Jülicher and U. Seifert, Phys. Rev. E **49**, 4728 (1994).
- [32] R. Lipowsky, Biophys. J. **64**, 1133 (1993).
- [33] F. Jülicher and R. Lipowsky, Phys. Rev. E **53**, 2670 (1996).
- [34] I. Derényi, F. Jülicher, and J. Prost, Phys. Rev. Lett. **88**, 238101 (2002).
- [35] U. Seifert, Adv. Phys. **46**, 13 (1997).
- [36] J. Hassinger, G. Oster, D. Drubin, and P. Rangamani, Biophys. J. **112**, 310a (2017).
- [37] N. Walani, J. Torres, and A. Agrawal, Proc. Natl. Acad. Sci. U.S.A. **112**, E1423 (2015).
- [38] L. V. Chernomordik and M. M. Kozlov, Nat. Struct. Mol. Biol. **15**, 675 (2008).
- [39] M. Arroyo and A. DeSimone, Phys. Rev. E **79**, 031915 (2009).
- [40] M. Doi, Journal of Physics: Condensed Matter **23**, 284118 (2011).
- [41] M. Arroyo, N. Walani, A. Torres-Sánchez, and D. Kaurin, in *The Role of Mechanics in the Study of Lipid Bilayers* (Springer International Publishing, 2018) pp. 287–332.
- [42] G. Salbreux, F. Jülicher, J. Prost, and A. Callan-Jones, Phys. Rev. Res. **4**, 033158 (2022).
- [43] A. Katchalsky and P. F. Curran, *Nonequilibrium Thermodynamics in Biophysics* (Harvard University Press, 1965).
- [44] L. Onsager, Phys. Rev. **37**, 405 (1931).
- [45] L. Onsager, Phys. Rev. **38**, 2265 (1931).
- [46] F. Jülicher, S. W. Grill, and G. Salbreux, Rep. Prog. Phys. **81**, 076601 (2018).
- [47] A. Torres-Sánchez, D. Millán, and M. Arroyo, Journal of Fluid Mechanics **872**, 218, 271 (2019).
- [48] A. Sahu, Y. A. Omar, R. A. Sauer, and K. K. Mandadapu, J. Comp. Phys. **407**, 109253 (2020).
- [49] L. D. Wittwer and S. Aland, Journal of Computational Physics: X **17**, 100126 (2023).
- [50] C. Hirt, A. Amsden, and J. Cook, J. Comp. Phys. **14**, 227 (1974).
- [51] U. Seifert, K. Berndl, and R. Lipowsky, Phys. Rev. A **44**, 1182 (1991).
- [52] F. Jülicher, A. Ajdari, and J. Prost, Rev. Mod. Phys. **69**, 1269 (1997).
- [53] J. Prost, F. Jülicher, and J. F. Joanny, Nat. Phys. **11**, 111 (2015).
- [54] J. Meixner, Ann. Phys. **43**, 244 (1943).
- [55] J. Kierzenka and L. F. Shampine, ACM Trans. Math. Softw. **27**, 299 (2001).
- [56] R. Ma and J. Berro, Biophysical Journal **120**, 52a (2021).
- [57] A. Agrawal and D. J. Steigmann, Biomechanics and Modeling in Mechanobiology **8**, 371 (2009).
- [58] E. Lauga and T. R. Powers, Reports on Progress in Physics **72**, 096601 (2009).
- [59] A. Zöttl and H. Stark, Journal of Physics: Condensed Matter **28**, 253001 (2016).
- [60] M. Schmitt and H. Stark, Physics of Fluids **28**, 012106 (2016).
- [61] J. S. Bois, F. Jülicher, and S. W. Grill, Phys. Rev. Lett. **106**, 028103 (2011).
- [62] M. Bonati, L. D. Wittwer, S. Aland, and E. Fischer-Friedrich, New Journal of Physics **24**, 073044 (2022).
- [63] M. Théry, A. Jiménez-Dalmaroni, V. Racine, M. Bornens, and F. Jülicher, Nature **447**, 493 (2007).
- [64] N. T. L. Rodrigues, S. Lekomtsev, S. Jananji, J. Kriston-Vizi, G. R. X. Hickson, and B. Baum, Nature **524**, 489 (2015).
- [65] J. Sedzinski, M. Biro, A. Oswald, J.-Y. Tinevez, G. Salbreux, and E. Paluch, Nature **476**, 462 (2011).
- [66] M. J. Lighthill, Commun. Pure Appl. Math. **5**, 109 (1952).
- [67] C. A. Whitfield and R. J. Hawkins, New J. Phys. **18**, 123016 (2016).
- [68] L. D. Wittwer and S. Aland, J. Comp. Phys. X **17**, 100126 (2023).
- [69] E. Kreyszig, *Introduction to differential geometry and Riemannian geometry* (University of Toronto Press, 1968).
- [70] A. Sahu, R. A. Sauer, and K. K. Mandadapu, Phys. Rev. E **96**, 042409 (2017).

Appendix A: Differential geometry of axisymmetric surfaces

1. Geometric surface properties

For axisymmetric surfaces described by $\mathbf{X}(u, \phi, t)$ given in Eq. (8), tangent vectors $\mathbf{e}_i = \partial_i \mathbf{X}$ and surface normal $\mathbf{n} = \mathbf{e}_u \times \mathbf{e}_\phi / |\mathbf{e}_u \times \mathbf{e}_\phi|$ are given by

$$\mathbf{e}_u = h \begin{pmatrix} \cos \psi \cos \phi \\ \cos \psi \sin \phi \\ -\sin \psi \end{pmatrix} \quad \mathbf{e}_\phi = r \begin{pmatrix} -\sin \phi \\ \cos \phi \\ 0 \end{pmatrix} \quad \mathbf{n} = \begin{pmatrix} \sin \psi \cos \phi \\ \sin \psi \sin \phi \\ \cos \psi \end{pmatrix} \quad (\text{A1})$$

The metric tensor $g_{ij} = (\partial_i \mathbf{X}) \cdot (\partial_j \mathbf{X})$ and its inverse $g^{ij} = (g_{ij})^{-1}$, as well as the curvature tensor $C_{ij} = -\mathbf{n} \cdot \partial_i \partial_j \mathbf{X}$ are diagonal and read

$$g_{ij} = \begin{pmatrix} g_{uu} & 0 \\ 0 & g_{\phi\phi} \end{pmatrix} = \begin{pmatrix} h^2 & 0 \\ 0 & r^2 \end{pmatrix} \quad (\text{A2})$$

$$C_{ij} = \begin{pmatrix} C_{uu} & 0 \\ 0 & C_{\phi\phi} \end{pmatrix} = \begin{pmatrix} h\psi' & 0 \\ 0 & r \sin \psi \end{pmatrix}, \quad (\text{A3})$$

where we used that $h^2 = r'^2 + z'^2$ (see Eqs. (12), (13), main text). From the metric tensor we can read off the surface area element

$$dA = \sqrt{g} ds^1 ds^2 = h r du d\phi. \quad (\text{A4})$$

The non-vanishing Christoffel symbols $\Gamma_{ij}^k = (\partial_i \partial_j \mathbf{X}) \cdot \mathbf{e}^k = \frac{1}{2} g^{kl} (\partial_i g_{lj} + \partial_j g_{li} - \partial_l g_{ij})$ are given by

$$\Gamma_{uu}^u = \frac{h'}{h} \quad \Gamma_{u\phi}^\phi = \Gamma_{\phi u}^\phi = \frac{h \cos \psi}{r} \quad \Gamma_{\phi\phi}^u = -\frac{r \cos \psi}{h}. \quad (\text{A5})$$

The definition of the covariant derivative

$$\nabla_i w_j = \partial_i w_j - \Gamma_{ij}^k w_k \quad (\text{A6})$$

implies for a vector field w_i with $\partial_\phi w_i = 0$ that

$$\nabla_u w_u = w'_u - \frac{w_u h'}{h} \quad (\text{A7})$$

$$\nabla_\phi w_\phi = \frac{r \cos \psi}{h} w_u \quad (\text{A8})$$

$$\nabla_u w_\phi = w'_\phi - \frac{h \cos \psi}{r} w_\phi \quad (\text{A9})$$

$$\nabla_\phi w_u = -\frac{h \cos \psi}{r} w_\phi. \quad (\text{A10})$$

Covariant derivatives of second rank tensors are defined by $\nabla_i T_{jk} = \partial_i T_{jk} - \Gamma_{ij}^l T_{lk} - \Gamma_{ik}^l T_{jl}$ and can be expressed on an axisymmetric surfaces using the expressions above.

2. Vector and tensor divergence

We provide for reference explicit expressions for the divergences

$$\text{div}(\mathbf{v}) = \mathbf{e}^i \cdot \partial_i \mathbf{v} = \nabla_i v^i + C_k^k v_n \quad \text{div}(\mathbf{T}) = \mathbf{e}^i \cdot \partial_i \mathbf{T} = \nabla_i t^i \quad (\text{A11})$$

of a vector and of a tension tensor field \mathbf{v} and \mathbf{T} , respectively, on an axisymmetric surface parameterised by mesh coordinates u, ϕ , and $h = \sqrt{r'^2 + z'^2}$ spatially constant. It is convenient to use normalized tangent basis vectors $\bar{\mathbf{e}}_u := \mathbf{e}_u/h$ and $\bar{\mathbf{e}}_\phi := \mathbf{e}_\phi/r$, with \mathbf{e}_i given in Eqs. (A1), to define the components by $\mathbf{v} = \bar{v}_i \bar{\mathbf{e}}_i + v_n \mathbf{n}$ and $\mathbf{T} = \bar{t}_{ij} \bar{\mathbf{e}}_i \otimes \bar{\mathbf{e}}_j + \bar{t}_{n,i} \bar{\mathbf{e}}_i \otimes \mathbf{n}$. Vector and tensor

divergence are then given by

$$\operatorname{div}(\mathbf{v}) = \frac{1}{hr} \partial_u (r \bar{v}_u) + \left(\frac{\psi'}{h} + \frac{\sin \psi}{r} \right) v_n \quad (\text{A12})$$

and

$$\bar{\mathbf{e}}_u \cdot \operatorname{div}(\mathbf{T}) = \frac{1}{hr} \partial_u (r \bar{t}_{uu}) + \frac{\psi'}{h} \bar{t}_{n,u} - \frac{\cos \psi}{r} \bar{t}_{\phi\phi} \quad (\text{A13})$$

$$\bar{\mathbf{e}}_\phi \cdot \operatorname{div}(\mathbf{T}) = \frac{1}{hr} \partial_u (r \bar{t}_{u\phi}) + \frac{\sin \psi}{r} \bar{t}_{n,\phi} + \frac{\cos \psi}{r} \bar{t}_{\phi u} \quad (\text{A14})$$

$$\mathbf{n} \cdot \operatorname{div}(\mathbf{T}) = \frac{1}{hr} \partial_u (r \bar{t}_{n,u}) - \frac{\psi'}{h} \bar{t}_{uu} - \frac{\sin \psi}{r} \bar{t}_{\phi\phi}. \quad (\text{A15})$$

Appendix B: Arbitrary Lagrangian-Eulerian (ALE) dynamics of metric and curvature tensors

Dynamic equation for the metric and curvature tensor of surfaces parameterized by ALE coordinates can be derived in two steps. First, we consider a general shape variation $\mathbf{X}(s^1, s^2) \rightarrow \mathbf{X}(s^1, s^2) + \delta\mathbf{X}(s^1, s^2)$ with $\delta\mathbf{X} = \delta X^i \mathbf{e}_i + \delta X_n \mathbf{n}$ in the definition of the corresponding fields in terms of \mathbf{X} . Using $\delta\mathbf{n} = -(\mathbf{n} \cdot \partial_i \delta\mathbf{X}) \mathbf{e}^i$ and evaluating derivatives of the basis vectors as $\nabla_i \mathbf{e}_j = -C_{ij} \mathbf{n}$ and $\nabla_i \mathbf{n} = C_i^j \mathbf{e}_j$ one finds [18]

$$\delta g_{ij} = \nabla_i \delta X_j + \nabla_j \delta X_i + 2C_{ij} \delta X_n \quad (\text{B1})$$

$$\delta C_{ij} = C_j^k \nabla_i \delta X_k + C_i^k \nabla_j \delta X_k + \delta X^k \nabla_k C_{ij} - \nabla_i \nabla_j \delta X_n + C_{ki} C_j^k \delta X_n. \quad (\text{B2})$$

The Jacobi formula $\delta g = g g^{ij} \delta g_{ij}$ provides an additional relation for the variator for the metric determinant g , which yields together with Eq. (B1)

$$\delta \sqrt{g} = \sqrt{g} (\nabla_k \delta X^k + C_k^k \delta X_n). \quad (\text{B3})$$

In the second step, we assume $\delta\mathbf{X}$ results from an explicit time-dependence as dictated by Eq. (2). Therefore, we substitute $\delta\mathbf{X} = (\mathbf{v} - \mathbf{q})\delta t$ in the variation identities above, where $\mathbf{q} = q^i \mathbf{e}_i$ corresponds to a general coordinate flow that depends on the chosen parameterization. This yields the dynamics equations

$$\partial_t g_{ij} = \nabla_i (v_j - q_j) + \nabla_j (v_i - q_i) + 2C_{ij} v_n \quad (\text{B4})$$

$$\partial_t C_{ij} = C_j^k \nabla_i (v_k - q_k) + C_i^k \nabla_j (v_k - q_k) + (v^k - q^k) \nabla_k C_{ij} - \nabla_i \nabla_j v_n + C_{ki} C_j^k v_n \quad (\text{B5})$$

$$\partial_t \sqrt{g} = \sqrt{g} [\nabla_k (v^k - q^k) + C_k^k v_n], \quad (\text{B6})$$

for surfaces with an arbitrary Lagrangian-Eulerian parameterization. Known expressions for pure Lagrangian or Eulerian parameterizations [18] are obtained by setting $q^i = 0$ or $q^i = v^i$, respectively.

Using Eqs. (A2), (A3), (A7), (A8) and $w_u = g_{uu} w^u = h^2 w^u$, Eq. (B4) implies on axisymmetric surfaces the dynamic equations

$$\partial_t h = [(v^u - q^u)h]' + v_n \psi' \quad (\text{B7})$$

$$\partial_t r = (v^u - q^u)h \cos \psi + v_n \sin \psi, \quad (\text{B8})$$

which recovers Eqs. (14) and (16) derived in the main text directly by evaluating $d\mathbf{X}(u, \phi, t)/dt = \mathbf{v}$. In a similar fashion, we find from the above relations explicit expression for the dynamics of tangent angle ψ and meridional curvature $C_u^u = \psi'/h$:

$$\partial_t \psi = (v^u - q^u) \psi' - \frac{v_n'}{h} \quad (\text{B9})$$

$$\partial_t C_u^u = \left[(v^u - q^u) \frac{\psi'}{h} \right]' - \left(\frac{\psi'}{h} \right)^2 v_n - \frac{1}{h} \left[\frac{v_n'}{h} \right]'. \quad (\text{B10})$$

Appendix C: Conservation laws on ALE-parameterized curved surfaces

In order to derive conservation laws on ALE-parameterized curved surfaces, one has to understand how quantities of the form

$$F(t) = \int_{\omega(t)} f(s^1, s^2, t) dA \quad (\text{C1})$$

evolve in time, where the integration domain $\omega(t)$ is a *coordinate region that parameterizes a fixed set of material elements* and $dA = \sqrt{g} ds^1 ds^2$ is the area element. By definition, the coordinates in ω will only be independent of time if Lagrangian material coordinates are used. In this case, $\frac{dF}{dt}$ only has a contribution from temporal changes of the integrand. For $F(t)$ to be conserved, $\frac{dF}{dt} = 0$, one consequently requires

$$\text{Lagrangian: } \int_{\omega_0} \partial_t (f \sqrt{g}) ds^1 ds^2 = 0. \quad (\text{C2})$$

With Eulerian coordinates in Eq. (C1), the integration domain $\Omega(t)$ of coordinates associated with a fixed set of material elements becomes explicitly time-dependent and we expect $\frac{dF}{dt}$ to pick up additional contributions. Instead of deriving these additional contributions, a physical argument is typically made that balances changes within a "fixed" area patch against fluxes across the integration boundary. Specifically, it is postulated that conservation of the quantity $F(t)$ for an Eulerian parameterization implies

$$\text{Eulerian: } \int_{\omega(t)} \partial_t (f \sqrt{g}) ds^1 ds^2 = - \oint_{\partial\omega(t)} f v^i \nu_i ds, \quad (\text{C3})$$

where ds is the arc length coordinate along the curve bounding the area of integration and $\boldsymbol{\nu} = \nu_i \mathbf{e}^i$ is the in plane unit normal of that curve. In the following, we show using an arbitrary Lagrangian-Eulerian parameterization that both Eqs. (C2) and (C3) arise as special cases from a single expression for $\frac{dF}{dt}$, with $F(t)$ given in Eq. (C1), when taking into account temporal changes of both the integrand and the integration domain.

1. Moving boundary integrals with ALE parameterization

To determine the total time derivative of $F(t)$ in Eq. (C1) for an ALE-parameterized surface, we have to approximate (denoting for brevity $\tilde{f} = f \sqrt{g}$)

$$F(t + \delta t) = \int_{\omega(t+\delta t)} \tilde{f}(\bar{s}^1, \bar{s}^2, t + \delta t) d\bar{s}^1 d\bar{s}^2, \quad (\text{C4})$$

to linear order in δt . The coordinate domains of integration at times t and $t + \delta t$ are parameterized by coordinates s^i and \bar{s}^i , respectively. These coordinates are related by

$$\begin{aligned} \bar{s}^i &= s^i(t + \delta t) \\ &= s^i(t) + \left. \frac{\partial s^i}{\partial t} \right|_S \delta t + \mathcal{O}(\delta t^2) \\ &= s^i + q^i \delta t + \mathcal{O}(\delta t^2), \end{aligned} \quad (\text{C5})$$

where the time derivative at fixed material coordinate S takes into account that we integrate at all times over a fixed set of material elements. The coordinate flow components $q^i = \partial_t s^i|_S$ are in principle arbitrary and may themselves depend on s^i . From Eq. (C5), it then follows that

$$\tilde{f}(\bar{s}^1, \bar{s}^2, t + \delta t) = \tilde{f}(s^1, s^2, t) + \left(\partial_t \tilde{f} + q^i \partial_i \tilde{f} \right) \delta t + \mathcal{O}(\delta t^2) \quad (\text{C6})$$

and

$$\begin{aligned} d\bar{s}^1 d\bar{s}^2 &= \det \left(\frac{\partial \bar{s}^i}{\partial s^j} \right) ds^1 ds^2 \\ &= (1 + \partial_i q^i \delta t) ds^1 ds^2 + \mathcal{O}(\delta t^2). \end{aligned} \quad (\text{C7})$$

Using Eqs. (C6) and (C7) in Eq. (C4) together with Eq. (C1), we find

$$F(t + \delta t) - F(t) = \delta t \int_{\Omega(t)} \left[\partial_t \tilde{f} + \tilde{f} \partial_i q^i + q^i \partial_i \tilde{f} \right] ds^1 ds^2 + \mathcal{O}(\delta t^2). \quad (\text{C8})$$

and therefore

$$\frac{dF}{dt} = \int_{\omega(t)} \left[\partial_t \tilde{f} + \partial_i (\tilde{f} q^i) \right] ds^1 ds^2. \quad (\text{C9})$$

Reintroducing $\tilde{f} = f \sqrt{g}$, and using $dA = \sqrt{g} ds^1 ds^2$ and $\partial_i \sqrt{g} = \sqrt{g} \Gamma_{ik}^k$ [69], Eq. (C9) yields

$$\frac{dF}{dt} = \int_{\omega(t)} \left[\frac{1}{\sqrt{g}} \partial_t (f \sqrt{g}) + \nabla_i (f q^i) \right] dA. \quad (\text{C10})$$

Equation (C10) holds for any parameterization described by the coordinate flow components q^i . In flat space ($g_{ij} = \delta_{ij} \Rightarrow \sqrt{g} = 1, \nabla_i \rightarrow \partial_i$) and with an Eulerian parameterization ($q^i = v^i$) Eq. (C10) is known as Reynolds transport theorem [70]. An alternative way of writing Eq. (C10) follows from using the metric determinant dynamics Eq. (B6), which yields

$$\begin{aligned} \frac{dF}{dt} &= \int_{\omega(t)} \left[\partial_t f + q^i \partial_i f + f (\nabla_k v^k + C_k^k v_n) \right] dA \\ &= \int_{\omega(t)} \left[\frac{df}{dt} + f \text{div}(\mathbf{v}) \right] dA, \end{aligned} \quad (\text{C11})$$

where we have used $\text{div}(\mathbf{v}) := \mathbf{e}^i \cdot \partial_i \mathbf{v} = \nabla_k v^k + C_k^k v_n$ and the definition of the total time derivative $\frac{d}{dt}(\cdot)$ for arbitrary Lagrangian-Eulerian coordinates [see also Eq. (2)]

$$\frac{df}{dt} := \partial_t f + q^i \partial_i f. \quad (\text{C12})$$

Note, that using Eq. (C11) with $f = 1$ the dynamics of the total surface area follows as

$$\frac{dA}{dt} = \int (\nabla_k v^k + C_k^k v_n) dA = \int \text{div}(\mathbf{v}) dA, \quad (\text{C13})$$

which is independent of the choice of the coordinate flow components q^i . Therefore, local area conservation on the surface can be realized by imposing $\text{div}(\mathbf{v}) = 0$, irrespective of the choice of parameterization and as done in Sec. V A via the Lagrange multiplier γ_H [see Eq. (50)]. The explicit expression of $\text{div}(\mathbf{v})$ on the cylindrical surface is given in Eq. (A12).

2. Generalized conservation laws and continuity equation

If $F(t)$ is a conserved quantity, we must have $\frac{dF}{dt} = 0$ and the right-hand side of Eq. (C10) can be rearranged into

$$\text{ALE: } \int_{\Omega(t)} \partial_t (f \sqrt{g}) ds^1 ds^2 = - \oint_{\partial\Omega(t)} f q^i \nu_i ds, \quad (\text{C14})$$

where we have used the covariant Stokes theorem [18]

$$\int_{\Omega} \nabla_i w^i dA = \oint_{\partial\Omega} w^i \nu_i ds. \quad (\text{C15})$$

For the special cases of Lagrangian material coordinates ($q^i = 0$) and Eulerian coordinates ($q^i = v^i$), we recover from the general expression (C14) the known expressions Eqs. (C2) and (C3). For any other parameterization choice, one still finds an effective "flux across the boundary" $\sim f \mathbf{q}$, which is however just an artefact of the parameterization and has no immediate physical interpretation.

a. *Mass conservation*

Using Eq. (C11) with $f = \rho$, where ρ is the mass area density, and imposing that total mass $F(t) = M(t)$ must be conserved, we find

$$\partial_t \rho + q^i \partial_i \rho + \rho \operatorname{div}(\mathbf{v}) = 0. \quad (\text{C16})$$

It is easy to check that mass conservation law Eq. (C16) takes the known forms when considering purely Lagrangian ($q^i = 0$) or purely Eulerian coordinates ($q^i = v^i$) [18]. On an axisymmetric surface, Eq. (C16) can be expressed as

$$\partial_t \rho + q^u \rho' + \frac{\rho}{hr} \partial_u (hrv^u) + \rho \left(\frac{\psi'}{h} + \frac{\sin \psi}{r} \right) v_n = 0, \quad (\text{C17})$$

where we used

$$\operatorname{div}(\mathbf{v}) = \frac{\partial_u (hrv^u)}{hr} + \left(\frac{\psi'}{h} + \frac{\sin \psi}{r} \right) v_n \quad (\text{C18})$$

on an axisymmetric surface. Equation (C17) is used in Secs. VB 1 and VB 2 to evolve a concentration field on the surface.

b. *Momentum conservation and force balance*

The total linear momentum of an arbitrarily parameterized patch of fixed material elements is given by

$$\mathbf{g} = \int_{\Omega(t)} \rho \mathbf{v} dA. \quad (\text{C19})$$

Momentum balance requires

$$\frac{d\mathbf{g}}{dt} = \oint_{\partial\Omega} \boldsymbol{\nu} \cdot \mathbf{T} ds + \int_{\Omega} \mathbf{f}^{\text{ext}} dA, \quad (\text{C20})$$

where $\mathbf{T} = \mathbf{e}_i \otimes \mathbf{t}^i$ is the tension tensor and \mathbf{f}^{ext} are external forces. Equation (C20) must hold for any fixed set of material elements. Hence, combining Eq. (C11), mass conservation Eq. (C16) and the covariant Stokes theorem Eq. (C15), momentum balance can be expressed as

$$\rho \mathbf{a} = \nabla_i \mathbf{t}^i + \mathbf{f}^{\text{ext}}, \quad (\text{C21})$$

where $\operatorname{div}(\mathbf{T}) = \nabla_i \mathbf{t}^i$ and

$$\mathbf{a} := \frac{d\mathbf{v}}{dt} = \partial_t \mathbf{v} + q^i \partial_i \mathbf{v} \quad (\text{C22})$$

is the local center-of-mass acceleration for an arbitrary Lagrangian-Eulerian parameterization. Explicit component expressions of $\nabla_i \mathbf{t}^i$ on axisymmetric surfaces, most relevant for the overdamped force balance considered in this work, are provided in Eqs. (A13)–(A15).

Alternatively, we can use Eq. (C10) to evaluate time derivative $\frac{d\mathbf{g}}{dt}$ with \mathbf{g} given in Eq. (C19) and find that momentum balance Eq. (C20) can be equivalently written as

$$\frac{1}{\sqrt{g}} \partial_t (\rho \mathbf{v} \sqrt{g}) = \operatorname{div}(\mathbf{T} - \rho \mathbf{q} \otimes \mathbf{v}) + \mathbf{f}^{\text{ext}}. \quad (\text{C23})$$

In the special case of an Eulerian parameterization, $q^i = v^i$, Eqs. (C20)–(C23) are equivalent to expressions in [18] and, in flat space ($g_{ij} = \delta_{ij} \Rightarrow \sqrt{g} = 1, \nabla_i \rightarrow \partial_i$), $\mathbf{T}_{\text{tot}} = \mathbf{T} - \rho \mathbf{v} \otimes \mathbf{v}$ is sometimes referred to as "total stress" [46].

c. *Torque balance*

For completeness, we provide component expression of the torque balance equation on axisymmetric surfaces. Specifically, Eq. (24) with $\mathbf{M} = \mathbf{e}_i \otimes \mathbf{m}^i$ can be written as

$$\nabla_i \mathbf{m}^i = \mathbf{t}^i \times \mathbf{e}_i. \quad (\text{C24})$$

The component expressions of $\nabla_i \mathbf{m}^i$ can be read off Eqs. (A13)–(A15), with (normalized) in-plane tension and normal force components replaced by the corresponding moment tensor components, $\bar{t}_{ij} \rightarrow \bar{m}_{ij}$ and $\bar{t}_n^i \rightarrow \bar{m}_n^i$. The vector on the right-hand side of Eq. (C24) has components

$$\bar{\mathbf{e}}_u \cdot (\mathbf{t}^i \times \mathbf{e}_i) = -\bar{t}_{n,\phi} \quad (\text{C25})$$

$$\bar{\mathbf{e}}_\phi \cdot (\mathbf{t}^i \times \mathbf{e}_i) = \bar{t}_{n,u} \quad (\text{C26})$$

$$\mathbf{n} \cdot (\mathbf{t}^i \times \mathbf{e}_i) = \bar{t}_{\phi u} - \bar{t}_{u\phi}, \quad (\text{C27})$$

where we have used [18]

$$\epsilon_{ij} := \mathbf{n} \cdot (\mathbf{e}_i \times \mathbf{e}_j) = \sqrt{g} \begin{pmatrix} 0 & 1 \\ -1 & 0 \end{pmatrix} \quad (\text{C28})$$

and $\sqrt{g} = hr$ in the axisymmetric surface.

d. *Chemical free energy dynamics*

The free energy density in the rest frame has a contribution from the number density

$$f_c = f_c(c^\alpha). \quad (\text{C29})$$

The free energy change rate

$$\begin{aligned} \frac{dF_c}{dt} &= \int \left(\frac{df_c}{dt} + \text{div}(\mathbf{v})f_c \right) dA \\ &= \int \left(\mu^\alpha \frac{dc^\alpha}{dt} + \text{div}(\mathbf{v})f_c \right) dA \\ &= \int [(f_c - \mu^\alpha c^\alpha) \text{div}(\mathbf{v}) - \mu^\alpha \text{div}(\mathbf{j}^\alpha) + (r_c^\alpha + J_n^\alpha) \mu^\alpha] dA, \end{aligned} \quad (\text{C30})$$

where $\mu^\alpha = \partial f_c / \partial c^\alpha$ is the chemical potential associated with the α species. When we perform variations against the velocity \mathbf{v} , Eq. (28) will contribute an equilibrium isotropic stress

$$\mathbf{T}_e = (f_c - \mu^\alpha c^\alpha) \mathbf{G} \equiv \gamma_e \mathbf{G}. \quad (\text{C31})$$

Appendix D: Equilibrium tension and moments

Equilibrium tensions and moments arising from the Helfrich energy Eq. (26) can alternatively be derived using the virtual work principle, which leads for arbitrary surface to [18]

$$t_e^{ij} = \frac{\kappa}{2} (C_k^k - C_0) ((C_k^k - C_0) g^{ij} - 2C^{ij}) \quad (\text{D1})$$

$$m_e^{ij} = \kappa (C_k^k - C_0) \epsilon^{ij}. \quad (\text{D2})$$

The normal component of the torque balance Eq. (C24) implies in this case that t_e^{ij} is symmetric. The in-plane component of Eq. (C24) yields normal forces of the form [18]

$$t_{n,e}^i = \kappa \nabla^i (C_k^k - C_0). \quad (\text{D3})$$

Flux	Force	Time reversal signature of the force
\mathbf{S}^{iso}	$\hat{\mathbf{T}}^{\text{iso}}$	+1
$\tilde{\mathbf{S}}$	$\tilde{\hat{\mathbf{T}}}_d$	+1
r_p	$\Delta\mu$	+1

Table VI. Conjugate variables in the entropy production rate

For C_0, κ constant and $\mathbf{T} = t_e^{ij} \mathbf{e}_i \otimes \mathbf{e}_j + t_{n,e}^i \mathbf{e}_i \otimes \mathbf{n}$ with tension and normal forces given in Eqs. (D1) and (D3) the tangential force balance $\mathbf{e}^j \cdot \text{div}(\mathbf{T}_e) = \nabla_i t_e^{ij} + C_i^j t_{n,e}^i = 0$ is identically satisfied. An inhomogeneous spontaneous curvature, as considered in Sec. V A, will in general contribute a force density to the tangential force balance.

On an axisymmetric surface the Helfrich energy Eq. (26) is given by $F_H = 2\pi \int_0^1 du (\gamma_H + f_\kappa) r h$ with

$$f_\kappa = \frac{\kappa}{2} \left(\frac{\sin \psi}{r} + \frac{\psi'}{h} - C_0 \right)^2. \quad (\text{D4})$$

Together with Eq. (C31) the full equilibrium tensor can then be expressed as

$$\begin{aligned} \mathbf{T}_e = & \gamma \mathbf{G} + \frac{\kappa}{2} \left[\left(\frac{\sin \psi}{r} - C_0 \right)^2 - \left(\frac{\psi'}{h} \right)^2 \right] \bar{\mathbf{e}}_u \otimes \bar{\mathbf{e}}_u + \frac{\kappa}{2} \left[\left(\frac{\psi'}{h} - C_0 \right)^2 - \left(\frac{\sin \psi}{r} \right)^2 \right] \bar{\mathbf{e}}_\phi \otimes \bar{\mathbf{e}}_\phi \\ & + \kappa \left[\frac{1}{h} \partial_u \left(\frac{\sin \psi}{r} + \frac{\psi'}{h} - C_0 \right) \right] \bar{\mathbf{e}}_u \otimes \mathbf{n}, \end{aligned} \quad (\text{D5})$$

where $\gamma = \gamma_e + \gamma_H$.

Appendix E: Equivalence between variational equations and force balance equations

1. Unconstrained functional with Eulerian parameterization

In the case of Eulerian parameterization $q^i = v^i$, the Rayleigh functional density (42) has dependencies $R[v_u, v_\phi, v_n, r_p]$. To prepare the computation of variational equations in this case, we split the strain rate tensor $\mathbf{S} = \tilde{\mathbf{S}} + \mathbf{S}^{\text{iso}}$ into its traceless part $\tilde{\mathbf{S}}$ in Eq. (29) and isotropic part $\mathbf{S}^{\text{iso}} = \frac{1}{2} \text{div}(\mathbf{v}) \mathbf{G}$. Using the constituted laws Eqs. (38) and (39), the entropy production rate per unit area in Eq. (40) can be written as

$$\hat{\theta}_{\text{int}} \equiv \hat{\mathbf{T}}_d : \mathbf{S} + r_p \Delta \hat{\mu} = A_{11} \mathbf{S}^{\text{iso}} : \mathbf{S}^{\text{iso}} + A_{22} \tilde{\mathbf{S}} : \tilde{\mathbf{S}} + A_{33} r_p^2 + 2A_{13} r_p \mathbf{G} : \mathbf{S}^{\text{iso}}, \quad (\text{E1})$$

where

$$A_{11} = 2 \left(\eta_b + \frac{\xi^2}{\Lambda} \right), \quad A_{22} = 2\eta, \quad A_{33} = \frac{1}{\Lambda}, \quad A_{13} = \frac{\xi}{\Lambda}. \quad (\text{E2})$$

For axisymmetric surface, the free energy change rate in Eq. (34) reads

$$\frac{dF}{dt} = 2\pi \int_0^1 \left[\partial_t f_H + \frac{f_H}{rh} \partial_t(rh) + \text{div}(\mathbf{v}) \gamma_e - r_p \Delta \mu + J_n^{\text{ext}} \right] rh du + 2\pi rh f_H q^u \Big|_{u=0}^{u=1} \quad (\text{E3})$$

$$= 2\pi \int_0^1 \left[\partial_t f_\kappa + \frac{f_\kappa}{rh} \partial_t(rh) + \text{div}(\mathbf{v}) \gamma - r_p \Delta \mu + J_n^{\text{ext}} \right] rh du + 2\pi rh f_\kappa q^u \Big|_{u=0}^{u=1}, \quad (\text{E4})$$

where $\gamma = \gamma_H + \gamma_e$ and the Rayleigh dissipation functional (see Eq. (43), main text) becomes

$$R(\mathbf{v}, r_p) = \left(\frac{1}{2} \hat{\theta}_{\text{int}} + \partial_t f_\kappa + \frac{f_\kappa}{rh} \partial_t(rh) + \text{div}(\mathbf{v}) \gamma - r_p \Delta \mu + J_n^{\text{ext}} \right) rh. \quad (\text{E5})$$

a. Meridional force balance

We first perform variations against normalized tangential velocity \bar{v}_u for the Rayleigh functional in Eq. (43)

$$\frac{1}{2\pi} \frac{\delta \mathcal{R}}{\delta \bar{v}_u} = \frac{\partial R}{\partial \bar{v}_u} - \frac{d}{du} \left[\frac{\partial R}{\partial \bar{v}'_u} \right] = 0 \quad (\text{E6})$$

With the identities

$$\frac{\partial \mathbf{S}^{\text{iso}}}{\partial \bar{v}_u} = \frac{\cos \psi}{2r} \mathbf{G} \quad \frac{\partial \mathbf{S}^{\text{iso}}}{\partial \bar{v}'_u} = \frac{1}{2h} \mathbf{G}, \quad (\text{E7})$$

and

$$\frac{\partial \tilde{\mathbf{S}}}{\partial \bar{v}_u} = -\frac{\cos \psi}{2r} \mathbf{A} \quad \frac{\partial \tilde{\mathbf{S}}}{\partial \bar{v}'_u} = \frac{1}{2h} \mathbf{A}, \quad (\text{E8})$$

where $\mathbf{A} = \bar{\mathbf{e}}_u \otimes \bar{\mathbf{e}}_u - \bar{\mathbf{e}}_\phi \otimes \bar{\mathbf{e}}_\phi$ is a traceless tensor, it is easy to verify that Eq. (E6) leads to

$$\begin{aligned} \frac{1}{2\pi r h} \frac{\delta \mathcal{R}}{\delta \bar{v}_u} &= A_{11} \mathbf{S}^{\text{iso}} : \frac{\partial \mathbf{S}^{\text{iso}}}{\partial \bar{v}_u} + A_{22} : \frac{\partial \tilde{\mathbf{S}}}{\partial \bar{v}_u} + A_{13} r_p \mathbf{G} : \frac{\partial \mathbf{S}^{\text{iso}}}{\partial \bar{v}_u} + \frac{\cos \psi}{r} \gamma \\ &\quad - \frac{1}{rh} \frac{d}{du} \left[\left(A_{11} \mathbf{S}^{\text{iso}} : \frac{\partial \mathbf{S}^{\text{iso}}}{\partial \bar{v}'_u} + A_{22} \tilde{\mathbf{S}} : \frac{\partial \tilde{\mathbf{S}}}{\partial \bar{v}'_u} + A_{13} r_p \mathbf{G} : \frac{\partial \mathbf{S}^{\text{iso}}}{\partial \bar{v}'_u} \right) rh + \gamma r \right] \\ &= \frac{\cos \psi}{2r} \hat{\mathbf{T}}_d^{\text{iso}} : \mathbf{G} - \frac{1}{rh} \frac{d}{du} \left[\frac{1}{2} r \hat{\mathbf{T}}_d^{\text{iso}} : \mathbf{G} \right] - \frac{\cos \psi}{2r} \tilde{\mathbf{T}}_d : \mathbf{A} - \frac{1}{rh} \frac{d}{du} \left[\frac{1}{2} r \tilde{\mathbf{T}}_d : \mathbf{A} \right] + \frac{\cos \psi}{r} \gamma - \frac{1}{rh} \frac{d}{du} (\gamma r) \\ &= \frac{\cos \psi}{r} (\bar{t}_d^{\text{iso}})_{\phi\phi} - \frac{1}{rh} \frac{d}{du} [r (\bar{t}_d^{\text{iso}})_{uu}] + \frac{\cos \psi}{r} (\bar{t}_d)_{\phi\phi} - \frac{1}{rh} \frac{d}{du} [r (\bar{t}_d)_{uu}] + \frac{\cos \psi}{r} \gamma - \frac{1}{rh} \frac{d}{du} (\gamma r) \\ &= -\bar{\mathbf{e}}_u \cdot \text{div}(\hat{\mathbf{T}}_d + \gamma \mathbf{G}) = 0, \end{aligned} \quad (\text{E9})$$

which is the tangential force balance equation in the u -direction. In the first step, we have decomposed the dissipative stress $\hat{\mathbf{T}}_d = \hat{\mathbf{T}}_d^{\text{iso}} + \tilde{\mathbf{T}}_d$ into its isotropic part $\hat{\mathbf{T}}_d^{\text{iso}} \equiv A_{11} \mathbf{S}^{\text{iso}} + A_{33} r_p \mathbf{G}$ and traceless part $\tilde{\mathbf{T}}_d \equiv A_{22} \tilde{\mathbf{S}}$. From the third to the fourth line we have used the fact that the normalized component of the dissipative stress $(\bar{t}_d^{\text{iso}})_{\phi\phi} = (\bar{t}_d^{\text{iso}})_{\phi\phi}$ and $(\bar{t}_d)_{uu} = -(\bar{t}_d)_{\phi\phi}$. In the last step we have used Eq. (A13).

b. Azimuthal force balance

Similarly, we can perform variations against \bar{v}_ϕ , which leads to the tangential force balance in the ϕ -direction,

$$\frac{1}{2\pi r h} \frac{\delta \mathcal{R}}{\delta \bar{v}_\phi} = \frac{1}{2\pi r h} \left(\frac{\partial R}{\partial \bar{v}_\phi} - \frac{d}{du} \left[\frac{\partial R}{\partial \bar{v}'_\phi} \right] \right) = -\bar{\mathbf{e}}_\phi \cdot \text{div}(\hat{\mathbf{T}}_d + \gamma \mathbf{G}) = 0 \quad (\text{E10})$$

where we have used Eq. (A14) and the identities

$$\frac{\partial \mathbf{S}^{\text{iso}}}{\partial \bar{v}_\phi} = \mathbf{0} \quad \frac{\partial \mathbf{S}^{\text{iso}}}{\partial \bar{v}'_\phi} = \mathbf{0} \quad (\text{E11})$$

and

$$\frac{\partial \tilde{\mathbf{S}}}{\partial \bar{v}_\phi} = -\frac{\cos \psi}{2r} \mathbf{B} \quad \frac{\partial \tilde{\mathbf{S}}}{\partial \bar{v}'_\phi} = \frac{1}{2h} \mathbf{B}, \quad (\text{E12})$$

where $\mathbf{B} = \bar{\mathbf{e}}_u \otimes \bar{\mathbf{e}}_\phi + \bar{\mathbf{e}}_\phi \otimes \bar{\mathbf{e}}_u$.

c. Normal force balance

We finally perform variations against the normal velocity v_n . In Eulerian descriptions, we have

$$\begin{aligned}\partial_t r &= v_n \sin \psi, \\ \partial_t z &= v_n \cos \psi, \\ \partial_t h &= \psi' v_n, \\ \partial_t \psi &= -\frac{1}{h} v_n'.\end{aligned}\tag{E13}$$

Along with the identities

$$\frac{\partial \mathbf{S}^{\text{iso}}}{\partial v_n} = \mathbf{C}^{\text{iso}}, \quad \frac{\partial \mathbf{S}^{\text{iso}}}{\partial v_n'} = \mathbf{0}\tag{E14}$$

and

$$\frac{\partial \tilde{\mathbf{S}}}{\partial v_n} = \tilde{\mathbf{C}}, \quad \frac{\partial \tilde{\mathbf{S}}}{\partial v_n'} = \mathbf{0},\tag{E15}$$

where $\mathbf{C} = \text{grad}(\mathbf{n})$ is the curvature tensor, \mathbf{C}^{iso} and $\tilde{\mathbf{C}}$ are the isotropic and traceless part of \mathbf{C} respectively. We can prove that

$$\frac{1}{rh} \frac{\delta R}{\delta v_n} = \frac{1}{rh} \left(\frac{\partial \mathcal{R}}{\partial v_n} - \frac{d}{du} \left[\frac{\partial \mathcal{R}}{\partial v_n'} \right] + \frac{d^2}{du^2} \left[\frac{\partial \mathcal{R}}{\partial v_n''} \right] \right) = -\mathbf{n} \cdot \text{div}(\hat{\mathbf{T}}_d + \mathbf{T}_e) = 0\tag{E16}$$

where \mathbf{T}_e given in Eq. (D5) is the equilibrium stress.

2. Constrained functional with SLE parameterization

If we introduce the Lagrangian multipliers α, β in Eq. (46) to impose geometric constraints the dependence of the Rayleigh functional density R on the normal velocity v_n is removed and it becomes a function $R[v^u, v^\phi, \partial_t r, \partial_t z, \partial_t h, \partial_t \psi, r_p]$. To prepare the computation of variational equations, we denote the strain-rate tensor \bar{v}_{ij} components with respect to the normalized basis by

$$\bar{v}_{uu} = \frac{1}{h} v_u' + \frac{\psi'}{h} v_n\tag{E17}$$

$$\bar{v}_{\phi\phi} = \frac{\cos \psi}{r} \bar{v}_u + \frac{\sin \psi}{r} v_n\tag{E18}$$

$$\bar{v}_{u\phi} = \frac{1}{2} \left(\frac{\bar{v}_\phi'}{h} - \frac{\cos \psi}{r} \bar{v}_\phi \right).\tag{E19}$$

The entropy production rate density in Eq. (40) given by $\hat{\mathbf{T}}_d : \mathbf{S} + r_p \Delta \hat{\mu} = S_1 + S_2 + S_3$ can be split into three parts

$$S_1 = \eta_b (\bar{v}_{uu} + \bar{v}_{\phi\phi})^2,\tag{E20}$$

$$S_2 = \eta [(\bar{v}_{uu} - \bar{v}_{\phi\phi})^2 + (2\bar{v}_{u\phi})^2],\tag{E21}$$

$$S_3 = \frac{1}{\Lambda} [r_p + \xi (\bar{v}_{uu} + \bar{v}_{\phi\phi})]^2,\tag{E22}$$

In the free energy change rate dF/dt in Eq. (34), we have

$$\frac{1}{\sqrt{g}} \partial_t (f_H \sqrt{g}) = \frac{1}{rh} \partial_t (f_H rh) = \partial_t f_H + f_H \frac{\partial_t (rh)}{rh},\tag{E23}$$

in which

$$\partial_t f_H = \frac{\partial f_H}{\partial r} \partial_t r + \frac{\partial f_H}{\partial \psi} \partial_t \psi + \frac{\partial f_H}{\partial \psi'} \partial_t \psi' + \frac{\partial f_H}{\partial h} \partial_t h. \quad (\text{E24})$$

The constrained Rayleigh functional density then becomes

$$\begin{aligned} \bar{R}(\mathbf{v}, r_p) = & \left[\frac{1}{2}(S_1 + S_2 + S_3) + \frac{1}{2}\Gamma(\bar{v}_u^2 + \bar{v}_\phi^2) + \gamma(\bar{v}_{uu} + \bar{v}_{\phi\phi}) + \partial_t f_H + f_H \frac{\partial_t(rh)}{rh} - r_p \Delta\mu \right] rh \\ & + \partial_t [\alpha(r' - h \cos \psi) + \beta(z' + h \sin \psi) + \zeta h'] - (f_n^{ext} v_n + f_u^{ext} \bar{v}_u + f_\phi^{ext} \bar{v}_\phi) rh. \end{aligned} \quad (\text{E25})$$

Note first that variation against r_p immediately yield

$$\frac{1}{\Lambda} [r_p + \xi(\bar{v}_{uu} + \bar{v}_{\phi\phi})] - \Delta\mu = 0, \quad (\text{E26})$$

which is equivalent to the constitutive law for the production rate r_p (Eq. (36), main text).

a. Meridional force balance

When performing variation against \bar{v}_u , we have

$$\frac{\partial R}{\partial \bar{v}_u} = [\eta_b(\bar{v}_{uu} + \bar{v}_{\phi\phi}) - \eta(\bar{v}_{uu} - \bar{v}_{\phi\phi}) + \gamma + \xi \Delta\mu] h \cos \psi + \Gamma v_u r h - f_u^{ext} r h \quad (\text{E27})$$

$$\frac{\partial R}{\partial \bar{v}_u'} = [\eta_b(\bar{v}_{uu} + \bar{v}_{\phi\phi}) + \eta(\bar{v}_{uu} - \bar{v}_{\phi\phi}) + \gamma + \xi \Delta\mu] r \quad (\text{E28})$$

$$-\frac{\partial R}{\partial \bar{v}_u} + \left[\frac{\partial R}{\partial \bar{v}_u'} \right]' = [\eta_b(\bar{v}_{uu} + \bar{v}_{\phi\phi}) + \eta(\bar{v}_{uu} - \bar{v}_{\phi\phi}) + \gamma + \xi \Delta\mu]' r + 2\eta(\bar{v}_{uu} - \bar{v}_{\phi\phi}) h \cos \psi - \Gamma \bar{v}_u r h + f_u^{ext} r h = 0 \quad (\text{E29})$$

Using

$$(\bar{t}_d)_{uu} = \eta_b(\bar{v}_{uu} + \bar{v}_{\phi\phi}) + \eta(\bar{v}_{uu} - \bar{v}_{\phi\phi}) + \gamma + \xi \Delta\mu, \quad (\text{E30})$$

and

$$(\bar{t}_d)_{\phi\phi} = \eta_b(\bar{v}_{uu} + \bar{v}_{\phi\phi}) - \eta(\bar{v}_{uu} - \bar{v}_{\phi\phi}) + \gamma + \xi \Delta\mu, \quad (\text{E31})$$

Eq. (E29) can be re-written as

$$\frac{[(\bar{t}_d)_{uu}]'}{h} + \frac{\cos \psi}{r} [(\bar{t}_d)_{uu} - (\bar{t}_d)_{\phi\phi}] = \Gamma \bar{v}_u - f_u^{ext}, \quad (\text{E32})$$

which is equivalent to the meridional force balance.

b. Azimuthal force balance

When performing variations against \bar{v}_ϕ , we have

$$\frac{\partial R}{\partial \bar{v}_\phi} = -2\eta(\bar{v}_{u\phi}) h \cos \psi + \Gamma \bar{v}_\phi r h \quad (\text{E33})$$

$$\frac{\partial R}{\partial \bar{v}_\phi'} = 2\eta(\bar{v}_{u\phi}) r \quad (\text{E34})$$

$$\begin{aligned}
-\frac{\partial R}{\partial \bar{v}_\phi} + \left[\frac{\partial R}{\partial \bar{v}'_\phi} \right]' &= 2\eta(\bar{v}_{u\phi})'r + 4\eta\bar{v}_{u\phi}h \cos \psi - \Gamma\bar{v}_\phi rh + f_\phi^{ext}rh \\
&= \eta \left[\frac{r^2}{h} \left[\frac{\bar{v}_\phi}{r} \right]' \right]' + \eta r \cos \psi \left[\frac{\bar{v}_\phi}{r} \right]' - \Gamma\bar{v}_\phi rh + f_\phi^{ext}rh = 0
\end{aligned} \tag{E35}$$

Using

$$(\bar{t}_d)_{u\phi} = 2\eta\bar{v}_{u\phi} \tag{E36}$$

we can rewrite Eq. (E35)

$$\frac{(\bar{t}_d)_{u\phi}}{h} + 2\frac{\cos \psi}{r}(\bar{t}_d)_{u\phi} = \Gamma v_\phi - f_\phi^{ext}. \tag{E37}$$

which corresponds to the azimuthal component of the force balance.

c. Normal force balance

When performing variations against $\partial_t r$, we have

$$\begin{aligned}
\frac{\partial R}{\partial(\partial_t r)} &= [\eta_b(\bar{v}_{uu} + \bar{v}_{\phi\phi}) + \xi\Delta\mu + \gamma] \left(\frac{\psi'}{h} + \frac{\sin \psi}{r} \right) \sin \psi rh \\
&\quad + \eta(\bar{v}_{uu} - \bar{v}_{\phi\phi}) \left(\frac{\psi'}{h} - \frac{\sin \psi}{r} \right) \sin \psi rh + \frac{\partial f_H}{\partial r} rh + f_H h - f_n^{ext} rh \sin \psi
\end{aligned} \tag{E38}$$

and

$$\frac{\partial R}{\partial(\partial_t r')} = \alpha \tag{E39}$$

Therefore

$$\begin{aligned}
-\frac{\partial R}{\partial(\partial_t r)} + \left[\frac{\partial R}{\partial(\partial_t r')} \right]' &= \alpha' - [\eta_b(\bar{v}_{uu} + \bar{v}_{\phi\phi}) + \xi\Delta\mu + \gamma] \left(\frac{\psi'}{h} + \frac{\sin \psi}{r} \right) \sin \psi rh \\
&\quad - \eta(\bar{v}_{uu} - \bar{v}_{\phi\phi}) \left(\frac{\psi'}{h} - \frac{\sin \psi}{r} \right) \sin \psi rh - \frac{\partial f_H}{\partial r} rh - f_H h + f_n^{ext} rh \sin \psi
\end{aligned} \tag{E40}$$

We can rewrite the normal force balance Eq. (E40) in the r -direction as

$$\alpha' = \left[(\bar{t}_d)_{uu} \frac{\psi'}{h} + (\bar{t}_d)_{\phi\phi} \frac{\sin \psi}{r} \right] rh \sin \psi + [(\bar{t}_e)_{\phi\phi}]r - f_n^{ext} rh \sin \psi \tag{E41}$$

When performing variations against $\partial_t z$, we have

$$\begin{aligned}
\frac{\partial R}{\partial(\partial_t z)} &= [\eta_b(\bar{v}_{uu} + \bar{v}_{\phi\phi}) + \xi\Delta\mu + \gamma] \left(\frac{\psi'}{h} + \frac{\sin \psi}{r} \right) rh \cos \psi \\
&\quad + \eta(\bar{v}_{uu} - \bar{v}_{\phi\phi}) \left(\frac{\psi'}{h} - \frac{\sin \psi}{r} \right) rh \cos \psi - f_n^{ext} rh \cos \psi
\end{aligned} \tag{E42}$$

and

$$\frac{\partial R}{\partial(\partial_t z')} = \beta \tag{E43}$$

Therefore

$$-\frac{\partial R}{\partial(\partial_t z)} + \left[\frac{\partial R}{\partial(\partial_t z')} \right]' = \beta' - [\eta_b(\bar{v}_{uu} + \bar{v}_{\phi\phi}) + \xi\Delta\mu + \gamma] \left(\frac{\psi'}{h} + \frac{\sin\psi}{r} \right) rh \cos\psi - \eta(\bar{v}_{uu} - \bar{v}_{\phi\phi}) \left(\frac{\psi'}{h} - \frac{\sin\psi}{r} \right) rh \cos\psi + f_n^{ext} rh \cos\psi \quad (\text{E44})$$

We can rewrite Eq. (E44) as

$$\beta' = \left[(\bar{t}_d)_{uu} \frac{\psi'}{h} + (\bar{t}_d)_{\phi\phi} \frac{\sin\psi}{r} \right] rh \cos\psi - f_n^{ext} rh \cos\psi \quad (\text{E45})$$

When performing variations against $\partial_t \psi$, we have

$$\frac{\partial R}{\partial(\partial_t \psi)} = \frac{\partial f_H}{\partial \psi} rh + \alpha h \sin\psi + \beta h \cos\psi \quad (\text{E46})$$

and

$$\frac{\partial R}{\partial(\partial_t \psi')} = \frac{\partial f_H}{\partial \psi'} rh \quad (\text{E47})$$

Therefore, we have

$$-\frac{\partial R}{\partial(\partial_t \psi)} + \left[\frac{\partial R}{\partial(\partial_t \psi')} \right]' = \left[\frac{\partial f_H}{\partial \psi'} rh \right]' - \frac{\partial f_H}{\partial \psi} rh - \alpha h \sin\psi - \beta h \cos\psi \quad (\text{E48})$$

When performing variations against $\partial_t h$, we have

$$\frac{\partial R}{\partial(\partial_t h)} = \frac{\partial f_H}{\partial h} rh + f_H r - \alpha \cos\psi + \beta \sin\psi \quad (\text{E49})$$

and

$$\frac{\partial R}{\partial(\partial_t h')} = \zeta \quad (\text{E50})$$

Therefore,

$$-\frac{\partial R}{\partial(\partial_t h)} + \left[\frac{\partial R}{\partial(\partial_t h')} \right]' = \zeta' - \frac{\partial f_H}{\partial h} rh - f_H r + \alpha \cos\psi - \beta \sin\psi \quad (\text{E51})$$

We take derivative of Eq. (E51) with respect to u and substitute α' in Eq. (E41), β' in Eq. (E45), ψ'' derived from Eq. (E48), as well as r' and z' in Eqs. (12) and (13). All together, it leads to the equation

$$\zeta'' = 0. \quad (\text{E52})$$

Together with the boundary condition $\zeta(0) = 0$ and $\zeta(1) = 0$, we get $\zeta = 0$ for all $u \in [0, 1]$.

We then solve Eqs. (E48) and (E51) to obtain

$$\alpha = [(\bar{t}_e)_u^n \sin\psi + (\bar{t}_e)_{uu} \cos\psi] r \quad (\text{E53})$$

and

$$\beta = [(\bar{t}_e)_u^n \cos\psi - (\bar{t}_e)_{uu} \sin\psi] r. \quad (\text{E54})$$

We substitute β expressed in Eq. (E54) into Eq. (E45) and obtain

$$[(\bar{t}_e)_u^n \cos\psi - (\bar{t}_e)_{uu} \sin\psi] h \cos\psi + [(\bar{t}_e)_u^n \cos\psi - (\bar{t}_e)_{uu} \sin\psi]' r = \left[(\bar{t}_d)_{uu} \frac{\psi'}{h} + (\bar{t}_d)_{\phi\phi} \frac{\sin\psi}{r} \right] rh \cos\psi \quad (\text{E55})$$

which can be rearranged as

$$\frac{[(\bar{t}_e)_u^n]'}{h} + \frac{\cos \psi}{r} (\bar{t}_e)_u^n - \frac{\sin \psi}{r} (\bar{t}_e)_{uu} - \tan \psi \left(\frac{[(\bar{t}_e)_{uu}]'}{h} + (\bar{t}_e)_u^n \frac{\psi'}{h} \right) - (\bar{t}_e)_{uu} \frac{\psi'}{h} = \left[(\bar{t}_d)_{uu} \frac{\psi'}{h} + (\bar{t}_d)_{\phi\phi} \frac{\sin \psi}{r} \right] \quad (\text{E56})$$

Using the tangential force balance for the equilibrium stress

$$\frac{[(\bar{t}_e)_{uu}]'}{h} + \frac{\cos \psi}{r} [(\bar{t}_e)_{uu} - (\bar{t}_e)_{\phi\phi}] + \frac{\psi'}{h} (\bar{t}_e)_u^n = 0, \quad (\text{E57})$$

we can simplify Eq. (E56) as

$$\frac{[(\bar{t}_e)_u^n]'}{h} + \frac{\cos \psi}{r} (\bar{t}_e)_u^n - [(\bar{t}_e)_{\phi\phi} + (\bar{t}_d)_{\phi\phi}] \frac{\sin \psi}{r} - [(\bar{t}_e)_{uu} + (\bar{t}_d)_{uu}] \frac{\psi'}{h} = -p \quad (\text{E58})$$

This is the normal force balance equation.

Appendix F: Boundary conditions from variations

1. Boundary conditions with Eulerian parameterization

The boundary terms for the variations computed in Sec. E 1 read

$$\frac{\partial \mathcal{R}}{\partial [(\bar{v}_u)']} \delta \bar{v}_u \Big|_{u=0}^{u=1} = 2\pi r \boldsymbol{\nu} \cdot (f_H \mathbf{G} + \mathbf{T}_d) \cdot \bar{\mathbf{e}}_u \delta \bar{v}_u \Big|_{u=0}^{u=1} \quad (\text{F1})$$

$$\frac{\partial \mathcal{R}}{\partial [(\bar{v}_\phi)']} \delta \bar{v}_\phi \Big|_{u=0}^{u=1} = 2\pi r \boldsymbol{\nu} \cdot (f_H \mathbf{G} + \mathbf{T}_d) \cdot \bar{\mathbf{e}}_\phi \delta \bar{v}_\phi \Big|_{u=0}^{u=1} \quad (\text{F2})$$

$$\left[\frac{\partial \mathcal{R}}{\partial [(v_n)']} - \frac{d}{du} \left(\frac{\partial \mathcal{R}}{\partial [(v_n)'']} \right) \right] \delta \bar{v}_n \Big|_{u=0}^{u=1} = 2\pi r \boldsymbol{\nu} \cdot \mathbf{T}_e \cdot \mathbf{n} \delta v_n \Big|_{u=0}^{u=1} \quad (\text{F3})$$

$$\frac{\partial \mathcal{R}}{\partial [(v_n)'']} \delta \bar{v}_n' \Big|_{u=0}^{u=1} = \frac{2\pi r}{h} \boldsymbol{\nu} \cdot \mathbf{M}_e \cdot \mathbf{n} \delta v_n' \Big|_{u=0}^{u=1}, \quad (\text{F4})$$

where $\mathbf{M}_e = m_e^{ij} \mathbf{e}_i \otimes \mathbf{e}_j$ with m_e^{ij} given in Eq. (D2).

2. Boundary conditions with SLE parameterization and geometric constraints

Note that the Rayleigh functional Eq. (43) contains an additional boundary term as consequence of the SLE parameterization, which will contribute to the boundary conditions. For the variations computed in Sec. E 2 they now read

$$\left[\frac{\partial \mathcal{R}}{\partial [(\bar{v}_u)']} + \frac{\partial (f_H q^u r h)}{\partial \bar{v}_u} \right] \delta \bar{v}_u \Big|_{u=0}^{u=1} = 2\pi r \boldsymbol{\nu} \cdot (f_H \mathbf{G} + \mathbf{T}_d) \cdot \bar{\mathbf{e}}_u \delta \bar{v}_u \Big|_{u=0}^{u=1} \quad (\text{F5})$$

$$\frac{\partial \mathcal{R}}{\partial [(\bar{v}_\phi)']} \delta \bar{v}_\phi \Big|_{u=0}^{u=1} = 2\pi r \boldsymbol{\nu} \cdot (f_H \mathbf{G} + \mathbf{T}_d) \cdot \bar{\mathbf{e}}_\phi \delta \bar{v}_\phi \Big|_{u=0}^{u=1} \quad (\text{F6})$$

$$\left[\frac{\partial \mathcal{R}}{\partial [(\partial_t r)']} + \frac{\partial (f_H q^u r h)}{\partial (\partial_t r)} \right] \delta (\partial_t r) \Big|_{u=0}^{u=1} = (\alpha - f_H r \cos \psi) \delta (\partial_t r) \Big|_{u=0}^{u=1} \quad (\text{F7})$$

$$\left[\frac{\partial \mathcal{R}}{\partial [(\partial_t z)']} + \frac{\partial (f_H q^u r h)}{\partial (\partial_t z)} \right] \delta (\partial_t z) \Big|_{u=0}^{u=1} = (\beta + f_H r \sin \psi) \delta (\partial_t z) \Big|_{u=0}^{u=1} \quad (\text{F8})$$

$$\frac{\partial \mathcal{R}}{\partial [(\partial_t \psi)']} \delta (\partial_t \psi) \Big|_{u=0}^{u=1} = 2\pi r \bar{\mathbf{e}}_u \cdot \mathbf{M}_e \cdot \bar{\mathbf{e}}_\phi \delta (\partial_t \psi) \Big|_{u=0}^{u=1}. \quad (\text{F9})$$